Journal of Earth Science, *Vol. 30*, *No. 5*, *p. 977–995*, *October 2019* *ISSN 1674-487X*
Printed in China
https://doi.org/10.1007/s12583-019-1015-5

Early–Middle Triassic Intrusions in Western Inner Mongolia, China: Implications for the Final Orogenic Evolution in Southwestern Xing-Meng Orogenic Belt

Min Liu[1, 2], **Shaocong Lai**[*1], **Da Zhang**[2], **Renzhi Zhu**[1], **Jiangfeng Qin**[1], **Yongjun Di**[2]
1. *State Key Laboratory of Continental Dynamics*, *Department of Geology*, *Northwest University*, *Xi'an* 710069, *China*
2. *School of Earth Sciences and Resources*, *China University of Geosciences*, *Beijing* 100083, *China*
Min Liu: https://orcid.org/0000-0002-9784-9996; Shaocong Lai: https://orcid.org/0000-0003-0629-2748

ABSTRACT: The end-Permian to Early–Middle Triassic magmatic rocks in Inner Mongolia can provide valuable insights into the relationships between the collisional processes and the magmatic responses during the final orogenic evolution of Xing-Meng orogenic belt (XMOB). This paper presents zircon U-Pb ages and Hf isotopes, whole rock geochemical and Sr-Nd-Pb isotopic data for the Early–Middle Triassic diabases and monzogranites from the Langshan area, southwestern XMOB. Our results suggest that the studied diabases and monzogranites were respectively formed during Early Triassic and Middle Triassic. The Early Triassic diabases are characterized by "arc-like" geochemical signatures, including enrichment in Rb, U and K, and depletion in Nb, Ta, P and Ti. They have negative to weak positive $\varepsilon_{Nd}(t)$ values (-3.1 to +1.5) and relatively high initial ratios of $^{208}Pb/^{204}Pb$ (35.968–37.346), $^{207}Pb/^{204}Pb$ (15.448–15.508) and $^{206}Pb/^{204}Pb$ (16.280–17.492), indicating a subduction-metasomatized enriched lithospheric mantle source. Their low Ba/Rb (2.72–6.56), Ce/Y (0.97–1.39) and $(Tb/Yb)_N$ ratios (1.31–1.45) suggest that the parental magma was likely originated from low degree partial melting of the phlogopite-bearing lherzolite in a spinel-stability field. The Middle Triassic monzogranites show high Sr/Y ratios, low MgO, Cr and Ni contents, high Zr/Sm ratios (40–64), negative zircon $\varepsilon_{Hf}(t)$ values (-25.8 to -8.8), as well as relatively flat heavy rare earth element patterns. They were likely derived from low degree partial melting of a moderately thickened ancient lower crust. The diabases and the slightly postdated high Sr/Y granites in this study represent the magmatic responses to the final orogenic evolution in the southwestern XMOB. Together with regional works, we propose that the slab break-off of the Paleo-Asian oceanic lithosphere following the terminal collision between the North China Craton and the South Mongolia terranes triggered asthenospheric upwelling, and the ongoing convergence further initiated moderately crustal thickening and uplift in the XMOB.

KEY WORDS: diabase, granite, high Sr/Y, Early–Middle Triassic, Xing-Meng orogenic belt, slab break-off.

0 INTRODUCTION

Accretionary orogens formed at sites of subduction of the oceanic lithosphere are ultimately involved in a collisional phase when plate subduction ceased (Cawood et al., 2009), leading to continental amalgamation/collision, slab break-off, crustal thickening and subsequent lithospheric delamination, accompanied by extensive and diverse magmatism (e.g., Condie et al., 2009; Ferrari, 2004). Consequently, identification of magmatic records in response to these processes can help us better understand the final orogenic evolution in an accretionary orogen.

The Central Asian orogenic belt (CAOB) (Fig. 1a) is one of the world's largest and best-preserved accretionary orogens (Wilde, 2015; Xiao et al., 2015, 2003; Windley et al., 2007; Jahn et al., 2000). The southeastern segment of the CAOB, which is also known as Xing-Meng orogenic belt (XMOB), was mainly constructed by the convergence between the South Mongolia terranes (SMT) to the north and the North China Craton (NCC) to the south, driven by the evolution of the Paleo-Asian Ocean from Neoproterozoic to Late Paleozoic (Zhao et al., 2018; Ma et al., 2017; Li et al., 2016a; Wilde, 2015; Xiao et al., 2015, 2003; Xu et al., 2013; Jian et al., 2010; Windley et al., 2007). The Solonker suture zone is widely considered to have marked the terminal closure of the Paleo-Asian Ocean during the end-Permian to Early–Middle Triassic (Li et al., 2017, 2016a; Xiao et al., 2015, 2003; Eizenhöfer et al., 2014; Schulmann and Paterson, 2011). However, unlike the well documented Paleozoic arc magmatism and oceanic sub-

*Corresponding author: shaocong@nwu.edu.cn

Manuscript received September 13, 2018.
Manuscript accepted December 20, 2018.

duction (e.g., Li et al., 2016b; Eizenhöfer et al., 2015, 2014; Xiao et al., 2015; Xu et al., 2013; Jian et al., 2010, 2008; Zhang et al., 2009a, b), origin and petrogenesis of the end-Permian to Early–Middle Triassic collision-related magmatism in the XMOB are still enigmatic. Recent studies propose that the end-Permian to Early Triassic magmatic rocks in Mandula and southeastern Xilinhot were generated in relation to the slab break-off following the terminal collision (Li et al., 2016a; Jian et al., 2010), and the Early–Middle Triassic high Sr/Y granitoids in Linxi and central Jilin were magmatic responses to the subsequent crustal thickening (Li et al., 2017; Wang et al., 2015a). However all those works were centered on the Solonker suture zone, the end-Permian to Early–Middle Triassic magmatism in southwestern XMOB receives much less attention.

In this study, we present new zircon U-Pb ages and Lu-Hf isotopes, whole rock geochemical and Sr-Nd-Pb isotopic data for the Early–Middle Triassic diabases and monzogranites in the Langshan area, southwestern XMOB (Fig. 1b). Our results, in combination with regional studies, enable us to propose that the studied diabases and the monzogranites were respectively generated in response to the slab break-off and the following crustal thickening during the final orogenic evolution in southwestern XMOB.

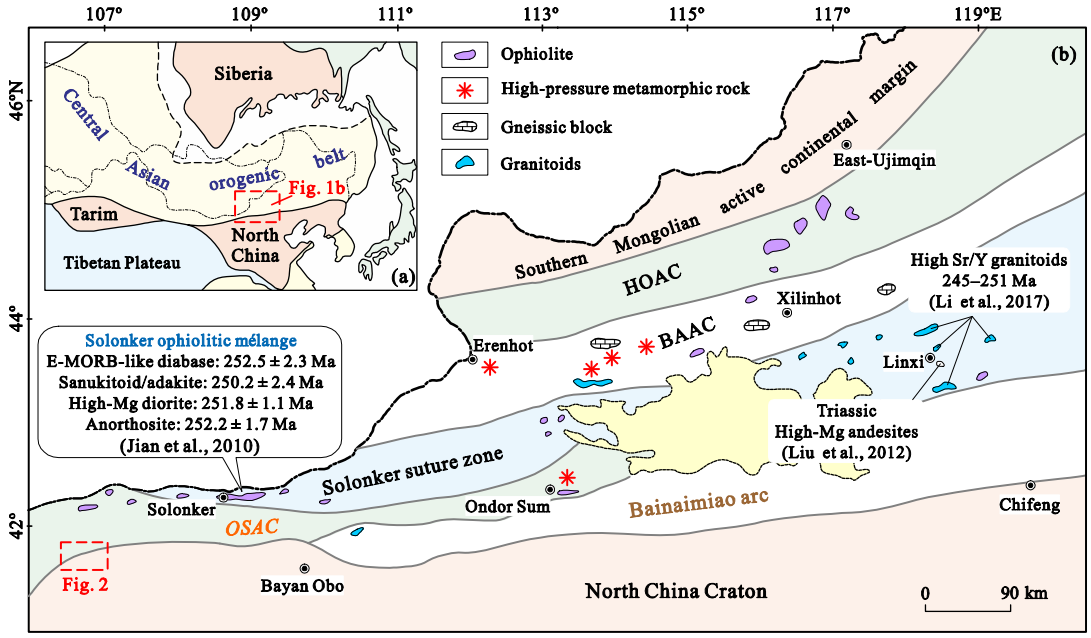

Figure 1. (a) Simplified sketch map of the Central Asian orogenic belt showing major tectonic sub-divisions of Central Asia (modified after Jahn et al., 2000); (b) geological sketch map of the central-western Xing-Meng orogenic belt (modified after Xiao et al., 2015; Jian et al., 2008). Abbreviations: OSAC. Ondor Sum subduction-accretionary complex; BAAC. Baolidao arc-accretionary complex; HOAC. Hegenshan ophiolite-accretionary complex.

1 GEOLOGICAL BACKGROUND AND SAMPLES

The XMOB has long been regarded as a complex collage of arcs, microcontinents, remnants of oceanic crust and associated volcanic-sedimentary sequences that amalgamated between the NCC and the SMT during the evolution and closure of the Paleo-Asian Ocean (e.g., Xiao et al., 2015, 2003; Jahn et al., 2000). The main part of the XMOB, from south to north, consists of the southern accretionary zone (SAZ) between the north margin of the NCC and the Solonker suture zone, the Solonker suture zone, the northern accretionary zone (NAZ) and the Hegenshan ophiolite-accretionary complex (Xiao et al., 2015; Jian et al., 2010). The SAZ includes the Early Paleozoic Bainaimiao arc (Zhang et al., 2014c) and the Ondor Sum subduction-accretion complex (Jian et al., 2008; de Jong et al., 2006; Xiao et al., 2003), the NAZ is characterized by the Paleozoic Baolidao arc-accretionary complex with accreted Precambrian blocks (e.g., Xilin Gol complex) (Xiao et al., 2015; Chen et al., 2009). The Hegenshan ophiolite-accretionary complex possesses a relatively complete lithological sequence (Miao et al., 2008), which is suggested to be formed in a subduction-related tectonic setting, such as back-arc or island arc-marginal basin, that related to the Early Carboniferous north-dipping subduction of the Paleo-Asian Ocean (Eizenhöfer et al., 2015; Miao et al., 2008; Robinson et al., 1999).

The Solonker suture zone, which strikes from the Solonker area to the Linxi area (Fig. 1b) (Xiao et al., 2015; Jian et al., 2010, 2008), marks the final closure of the Paleo-Asian Ocean in the southeastern CAOB (e.g., Li et al., 2017, 2016a; Zhang et al., 2017; Eizenhöfer et al., 2015, 2014; Wilde, 2015; Xiao et al., 2015, 2003). The ages of the tectonic mélanges and ophiolitic fragments that discontinuously distributed along the Solonker suture zone are consistently Early Permian (Song et al., 2015; Jian et al., 2010). The Middle Permian Zhesi Formation volcaniclastic and turbiditic strata in the Solonker suture zone are unconformably overlain by the Late Permian–Early Triassic Linxi Formation clastic rocks, which are considered to be accumulated in a terrestrial setting (Eizenhöfer et al., 2015; Li et al., 2014). Zhang et al. (2016a) suggests that the Solonker suture zone underwent intermediate-to-low *P*/*T* type metamorphism during the Triassic. Several end-Permian to Early–Middle Triassic collision-related granitoids also have been identified in the Linxi area (Li et al., 2017, 2016a).

The Langshan area in southwestern XMOB is approximately 100 km south of the Solonker suture zone (Fig. 1b). The Paleozoic tectonic affinity of the Langshan area was disputed because of the controversial relationship between the NCC and the Alxa Block (Zhang et al., 2016b; Yuan and Yang, 2015). Many recent studies have revealed that the Alxa Block had collided with the NCC before the Late Paleozoic (e.g., Wang et al., 2016; Zhang et al., 2016b), although the accurate timing and location of this amalgamation are still in debate. The eldest rocks in the Langshan area is the Archean high-grade metamorphic complex (Fig. 2), which are dominated by amphibolite, quartz schist and schistose to magmatic gneiss with granitic gneiss of 2 563 and 2 619 Ma (Liu, 2012). The Proterozoic basement rocks in the Langshan area mainly consist of greenschist-amphibolite facies metamorphosed carbonates, clastic rocks, with some Neoproterozoic meta-volcanic interlayers (Hu et al., 2014; Peng et al., 2010). Outcrops of the Paleozoic stratigraphy are only limited to the west of the Langshan area. They are mainly composed of some Carboniferous–Permian marine sedimentary and volcanic rocks, and are uncomfortably covered by the Jurassic–Quaternary sedimentary strata (Fig. 2). The Langshan area is also characterized by a complicated framework of Mesozoic multi-stage strike-slip faults and thrusts, which are interpreted to be related to the intraplate deformation phases across the southern CAOB (Zhang et al., 2016b, 2013; Darby and Ritts, 2007).

Igneous rocks in the Langshan area are mainly composed of the Late Paleozoic and Early Mesozoic felsic intrusions (Fig. 2) (e.g., Liu et al., 2016; Wang et al., 2015b; Lin et al., 2014; Peng et al., 2013), such as the ~338 Ma Baoribu quartz diorite with $\varepsilon_{Hf}(t)$ values of -6.9 to +2.0 in the north Chaoge Ondor (Liu et al., 2016), the ~281 Ma deformed granitic porphyry in the Urad Houqi area (Lin et al., 2014), and the ~259 Ma granodiorite with $\varepsilon_{Nd}(t)$ values of -2.7 ~ -1.6 close to the Huogeqi ore district (Wang et al., 2015b). Additionally, some small outcrops of the Early Paleozoic granitoids and the Late Paleozoic mafic intrusions are also observed (e.g., Liu et al., 2016; Wang et al., 2016, 2015b).

The investigated diabases are located immediately to the east of the Chaoge Ondor (Fig. 2), most of them are vertical and NE-SW trending. They intruded into the Late Paleozoic granitic rocks (Fig. 3a) and the Proterozoic greenschist-amphibolite facies metamorphic clastic rocks (Zhaertai Group), but did not penetrate the Mesozoic granitoids in the field. The intrusive contacts are very clear and thermal recrystallization can be observed near the boundary of most dykes. In contrast to their country rocks, the diabases are rarely subjected to metamorphism and deformation. Individual diabase dykes in the Langshan area typically have widths of 0.8 to 3.0 m and can be traced for distances of 0.2 to 8 km. The investigated monzogranites are located approximately 15 km west of Chaoge Ondor, with surface outcrops over 60 km^2 (Figs. 2 and 3b). They mainly intruded into the Early Carboniferous quartz diorite in the field, and are devoid of any effects of metamorphism or deformation. The diabases display ophitic or sub-ophitic textures, with similar mineral compositions of lath-shaped plagioclase (50 vol.%–60 vol.%) and pyroxene (30 vol.%–40 vol.%), with minor hornblende (~5 vol.%) and Fe-Ti oxides (Fig. 3c). The monzogranite is composed of plagioclase (25 vol.%–30 vol.%), K-feldspar (30 vol.%–35 vol.%), quartz (25 vol.%–30 vol.%), biotite (3 vol.%–10 vol.%) and minor accessory minerals (e.g., magnetite, zircon and apatite) (Fig. 3d).

2 ANALYTICAL METHODS

Zircon grains were separated from the whole-rock samples by standard techniques of density and magnetic methods and further purified by hand-picking using a binocular microscope. The internal structures of each grain were revealed by Cathodoluminescence (CL) imaging prior to the U-Pb analysis.

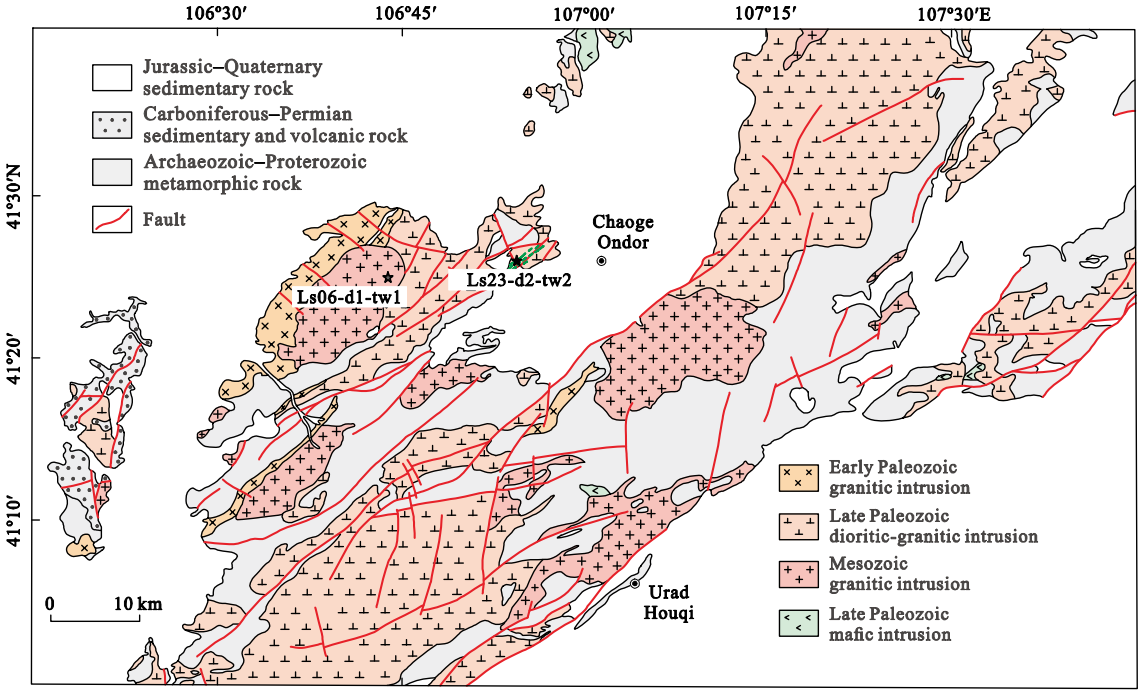

Figure 2. Geological sketch map of the Langshan area (modified after Liu et al., 2016).

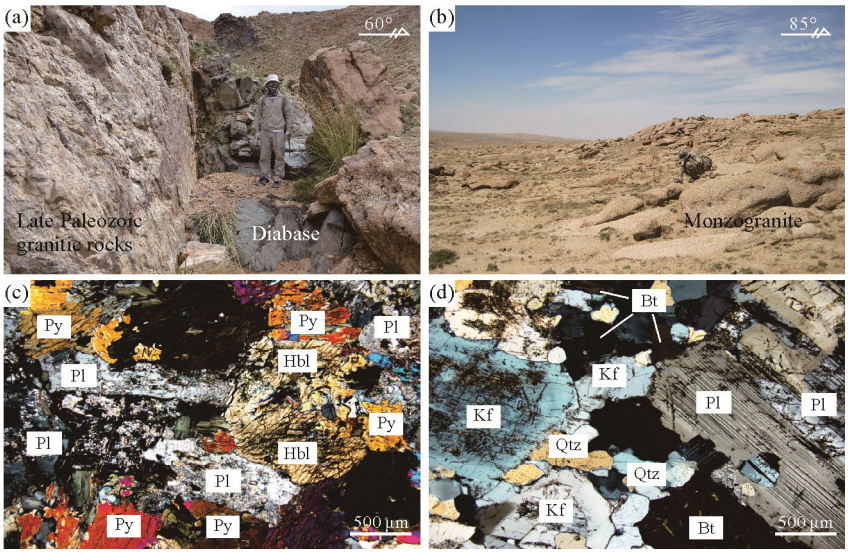

Figure 3. Representative field photographs and micrographs of the studied diabase and monzogranite from the Langshan area. Mineral abbreviations: Py. pyroxene; Hbl. hornblende; Pl. plagioclase; Kf. K-feldspar; Bt. biotite; Qtz. quartz.

Zircon U-Pb analysis for sample Ls23-d2-tw2 was carried out at the State Key Laboratory of Continental Dynamics, Northwest University, Xi'an, China, by using an Agilent 7500a ICP-MS equipped with a 193 nm laser, the spot size is 35 μm. Zircon U-Pb age analysis for sample Ls06-d1-tw1 was carried out on a Finnigan Neptune ICP-MS that equipped with New Wave 193 nm excimer lasers, at the Tianjin Institute of Geology and Mineral Resources, Tianjin, China. A 35 μm diameter spot was used for the laser ablation of a single zircon grain. The $^{206}Pb/^{238}U$ and $^{207}Pb/^{206}Pb$ ratios were calculated by the GLITTER program and corrections were applied using Harvard zircon 91500 as an external calibration. Details of the analytical methodology are described by Li et al. (2009) and Yuan et al. (2004). The common Pb corrections were made following the method of Andersen (2002). Isoplot 3.0 program (Ludwig, 2003) was used for data processing.

Whole-rock geochemical compositions were determined at the Analytical Laboratory of the Beijing Research Institute of Uranium Geology (BRIUG), China. Major elements were analysed on fused glass discs by a Philips PW2404 X-ray fluorescence spectrometry with analytical errors better than 1%–5%, FeO contents were determined using the classical wet chemical method. Trace elements were determined by using a Perkin-Elmer Sciex ELAN DRC-e inductively coupled plasma mass spectrometer (ICP-MS) and the analytical uncertainties were mostly better than 5%. Analytical procedures and instrument parameters were similar to those described by Gao et al. (2002).

The whole rock Sr-Nd and Pb isotopic analysis were performed on triton thermal ionization mass spectrometer (TIMS) and MAT261 TIMS, respectively, at the Central-South China Supervision and Inspection Center of Mineral Resources, Ministry of Land and Resources, Wuhan, China. The mass fractionation of Sr isotopic ratios has been exponentially corrected to the $^{86}Sr/^{88}Sr$=0.119 4 and Nd isotopic ratios to $^{146}Nd/^{144}Nd$= 0.721 9. The values for the NBS 987 Sr-standard and the BCR-2 Nd-standard measured during the data acuisition were $^{87}Sr/^{86}Sr$=0.710 31±4 (2σ) and $^{143}Nd/^{144}Nd$=0.512 62±5 (2σ), respectively. Repeated analysis yielded the $^{208}Pb/^{206}Pb$, $^{207}Pb/^{206}Pb$ and $^{204}Pb/^{206}Pb$ ratios of the Standard NBS981 in this study were 2.164 91±13 (2σ), 0.914 37±5 (2σ) and 0.059 104±5 (2σ), respectively. Detailed descriptions of the analytical techniques are given by Zeng et al. (2013).

In-situ zircon Lu-Hf isotopic analysis was conducted by using a Nu Plasma II MC-ICP-MS coupled with a Resolution M-50 193 nm laser at the State Key Laboratory of Continental Dynamics, Northwest University, Xi'an, China. A 44 μm laser beam with a repetition rate of 6 Hz was used for the analysis. Detailed information of these instruments and analytical technique can be found in Bao et al. (2017) and Yuan et al. (2008). The 91500 and MT standards yielded weighted $^{176}Hf/^{177}Hf$ ratios of 0.282 264±0.000 030 and 0.282 528±0.000 019, respectively.

3 RESULTS

3.1 Zircon U-Pb Ages

Zircons selected from diabase sample Ls23-d2-tw2 and monzogranite sample Ls06-d1-tw1 are mostly subhedral to euhedral, colourless or buff to transparent, with lengths of 50–200 μm. The majority of zircon grains exhibit clearly oscillatory zoning in the CL images (Fig. 4), suggesting their magmatic origin (Hoskin and Schaltegger, 2003). The Th/U ratios of zircons from Ls23-d2-tw2 and Ls06-d1-tw1 range from 0.04–1.34 and 0.06–0.42, respectively. Detailed zircon U-Pb isotopic data are presented in Table 1. Twenty-one spots were conducted on zircons from sample Ls23-d2-tw2, and most of them are located below the concordia line (Fig. 5a). However, four relatively younger zircon grains have concordant ages that range from 248 to 255 Ma and yield a weighted mean $^{206}Pb/^{238}U$ age of 251.4±3.6 Ma, and other five grains have concordant ages ranging from 271 to 273 Ma, yielding a concordant age of 272.1±1.6 Ma (Fig. 5b). A total of twenty-five spots of zircons from the monzogranite sample Ls06-d1-tw1 show nearly concordant ages and yield a well-weighted mean $^{206}Pb/^{238}U$ age of 245.5±0.7 Ma (Figs. 5c–5d), which means

Table 1 LA-ICP-MS U-Pb isotopic data for the zircons from the studied diabase and monzogranite samples

No.	Isotopic ratios							Ages (Ma)					
	Th/U	$^{206}Pb/^{238}U$	1σ	$^{207}Pb/^{235}U$	1σ	$^{207}Pb/^{206}Pb$	1σ	$^{206}Pb/^{238}U$	1σ	$^{207}Pb/^{235}U$	1σ	$^{207}Pb/^{206}Pb$	1σ
Ls23-d2-tw2 (N41º25′46″/E106º54′02″)													
1	0.68	0.039 80	0.000 50	0.279 70	0.013 40	0.050 90	0.002 50	252	3	250	11	238	117
2	1.26	0.043 00	0.000 80	0.308 50	0.020 20	0.052 10	0.003 60	271	5	273	16	288	117
3	0.91	0.040 30	0.000 60	0.277 20	0.012 10	0.049 90	0.002 40	255	4	248	10	188	74
4	0.73	0.039 60	0.000 60	0.282 90	0.021 80	0.051 90	0.004 10	250	4	253	17	280	180
5	0.29	0.328 60	0.003 70	5.492 70	0.067 90	0.121 20	0.002 60	1 832	18	1 899	11	1 974	10
6	0.71	0.065 90	0.000 90	0.528 10	0.018 50	0.058 20	0.002 30	411	6	431	12	536	52
7	0.45	0.043 20	0.000 60	0.315 60	0.010 30	0.053 00	0.002 00	273	3	279	8	330	50
8	0.68	0.039 20	0.000 60	0.296 00	0.015 20	0.054 70	0.003 00	248	4	263	12	401	86
9	1.34	0.122 70	0.001 70	1.140 80	0.033 80	0.067 50	0.002 30	746	10	773	16	852	39
10	0.04	0.090 90	0.001 00	0.938 50	0.014 90	0.074 90	0.001 50	561	6	672	8	1 065	40
11	0.68	0.043 30	0.000 60	0.355 60	0.010 80	0.059 60	0.002 10	273	3	309	8	591	43
12	0.6	0.067 80	0.000 80	0.524 50	0.010 80	0.056 10	0.001 50	423	5	428	7	456	26
13	0.72	0.071 20	0.000 80	0.592 80	0.010 40	0.060 40	0.001 50	444	5	473	7	617	20
14	1.08	0.197 50	0.002 20	2.696 00	0.035 20	0.099 00	0.002 20	1 162	12	1 327	10	1 606	11
15	0.63	0.212 00	0.002 80	2.646 30	0.081 30	0.090 50	0.003 00	1 240	15	1 314	23	1 437	65
16	0.51	0.043 00	0.000 70	0.334 10	0.016 80	0.056 40	0.003 10	271	4	293	13	467	83
17	0.14	0.095 40	0.001 10	1.015 80	0.019 80	0.077 20	0.002 00	588	7	712	10	1 127	21
18	0.71	0.043 00	0.000 60	0.326 80	0.015 20	0.055 10	0.002 70	271	4	287	12	416	111
19	0.44	0.186 10	0.002 20	2.095 90	0.046 20	0.081 70	0.002 00	1100	12	1 147	15	1 238	50
20	0.68	0.337 40	0.004 30	5.418 60	0.097 20	0.116 50	0.002 90	1874	21	1 888	15	1 903	16
Ls06-d1-tw1 (N41º26′16″/E106º44′30″)													
1	0.91	0.038 77	0.000 36	0.280 13	0.009 80	0.052 41	0.001 88	245	2	251	9	303	82
2	0.73	0.038 82	0.000 36	0.273 59	0.005 48	0.051 12	0.000 89	246	2	246	5	246	40
3	0.29	0.038 93	0.000 31	0.276 62	0.008 70	0.051 53	0.001 62	246	2	248	8	265	72
4	0.71	0.038 78	0.000 40	0.273 56	0.019 43	0.051 16	0.003 77	245	3	246	17	248	170
5	0.45	0.038 84	0.000 37	0.275 39	0.020 03	0.051 42	0.003 68	246	2	247	18	260	164
6	0.68	0.039 14	0.000 30	0.277 27	0.005 75	0.051 38	0.001 00	248	2	248	5	258	45
7	1.34	0.038 43	0.000 23	0.454 56	0.009 99	0.085 79	0.001 80	243	1	380	8	1 333	41
8	0.04	0.039 42	0.000 24	0.275 38	0.005 73	0.050 66	0.000 99	249	2	247	5	226	45
9	0.68	0.038 24	0.000 28	0.280 37	0.009 66	0.053 17	0.001 72	242	2	251	9	336	73
10	0.6	0.038 95	0.000 23	0.279 60	0.006 37	0.052 07	0.001 17	246	1	250	6	288	51
11	0.72	0.038 98	0.000 23	0.279 26	0.006 01	0.051 96	0.001 10	246	1	250	5	284	49
12	1.08	0.038 76	0.000 24	0.278 24	0.005 40	0.052 07	0.000 99	245	2	249	5	288	43
13	0.63	0.039 05	0.000 24	0.280 64	0.007 87	0.052 12	0.001 43	247	2	251	7	291	63
14	0.51	0.038 82	0.000 25	0.274 83	0.012 22	0.051 34	0.002 25	246	2	247	11	256	101
15	0.14	0.038 92	0.000 22	0.275 04	0.004 93	0.051 25	0.000 92	246	1	247	4	252	41
16	0.71	0.038 66	0.000 24	0.273 00	0.014 41	0.051 21	0.002 68	245	2	245	13	250	121
17	0.44	0.038 96	0.000 22	0.282 89	0.003 31	0.052 66	0.000 60	246	1	253	3	314	26
18	0.35	0.038 87	0.000 23	0.273 73	0.006 22	0.051 08	0.001 13	246	1	246	6	244	51
19	0.32	0.038 91	0.000 26	0.278 55	0.016 33	0.051 92	0.003 02	246	2	250	15	282	133
20	0.28	0.038 90	0.000 22	0.280 12	0.006 36	0.052 23	0.001 16	246	1	251	6	295	51
21	0.22	0.038 34	0.000 22	0.282 48	0.006 86	0.053 44	0.001 27	243	1	253	6	348	54
22	0.06	0.038 69	0.000 25	0.275 32	0.010 41	0.051 62	0.001 93	245	2	247	9	268	86
23	0.31	0.038 34	0.000 22	0.413 30	0.012 61	0.078 18	0.002 32	243	1	351	11	1 151	59
24	0.4	0.038 93	0.000 26	0.273 36	0.016 08	0.050 93	0.002 95	246	2	245	14	237	133
25	0.42	0.039 02	0.000 23	0.279 43	0.007 54	0.051 94	0.001 39	247	1	250	7	283	61

that emplacement of the studied monzogranite took place in the Middle Triassic.

3.2 Major and Trace Elements

The major and trace element concentrations of studied diabase and monzogranite samples are listed in Table 2. The relatively low LOI (loss on ignition) values of most samples indicate a limited degree of hydrothermal alteration.

The diabase samples have SiO_2 contents of 51.13 wt.%–54.55 wt.%, K_2O contents of 0.76 wt.%–1.84 wt.% and Na_2O contents of 2.56 wt.%–4.23 wt.%. They plot in the compositional fields of gabbro, gabbroic diorite, monzogabbro and monzodiorite (Fig. 6a) in the TAS diagram, and belong to the calc-alkaline series (Figs. 6b–6d). These characteristics are similar to those of the ~250 Ma E-MOEB-like diabase from the Solonker ophiolitic mélanges (Jian et al., 2010). In the Harker diagrams, they exhibit regular trends of decreasing Al_2O_3, Na_2O, K_2O, TiO_2 and P_2O_5 contents with increasing MgO contents (Fig. 7). All the studied diabase samples show similar rare earth element (REE) compositions, with total REE contents ranging from 74.7 ppm to 135.0 ppm. In the chondrite-normalized REE diagram (Fig. 8a), they are characterized by light REE (LREE) enrichment and slightly negative to positive Eu anomalies, with $(La/Yb)_N$ of 2.99–4.14 and Eu/Eu* of 0.88–1.17. Their primitive mantle-normalized trace element patterns (Fig. 8b) are generally characterized by enrichment in large ion lithophile elements (LILE; e.g., Rb, U, K, Pb) and depletion in high field strength elements (HFSE; e.g., Nb, Ta, P, Ti), which are similar to those of the "arc-like" magmatic rocks from the subduction zone (Ma et al., 2014).

The monzogranite samples exhibit relatively high SiO_2 (70.09 wt.%–72.63 wt.%), Na_2O (3.98 wt.%–4.08 wt.%), K_2O (3.76 wt.%–4.67 wt.%) and low $Fe_2O_3^T$ (1.54 wt.%–2.27 wt.%), MgO (0.40 wt.%–0.87 wt.%), TiO_2 (0.25 wt.%–0.33 wt.%) contents and $Mg^{\#}$ (100×MgO/(MgO+TFeO)) values (31.6–40.5). These rocks belong to high-K calc-alkaline series, and are metaluminous to weakly peraluminous with A/CNK ratios of 0.99–1.01. They also have relatively high concentrations of Al_2O_3 (14.10 wt.%–15.07 wt.%), Sr (310 ppm–380 ppm) but low Y (7.16 ppm–10.50 ppm) and Yb (0.60 ppm–1.15 ppm)

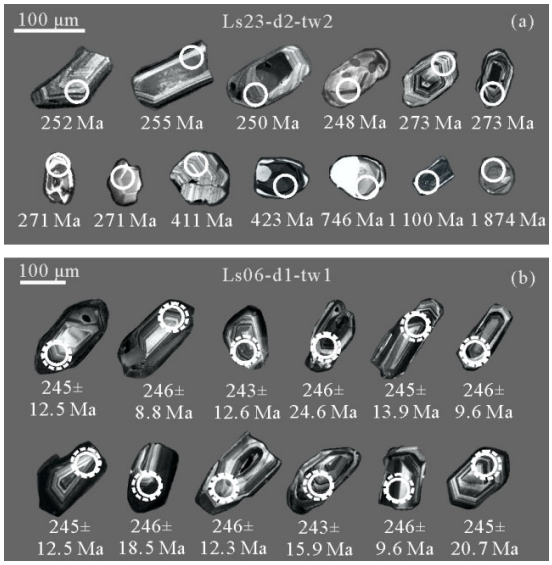

Figure 4. (a), (b) CL images of representative zircons from the studied diabases and (c) monzogranites. The solid and dotted circles denote the spots for U-Pb dating and Lu-Hf, respectively.

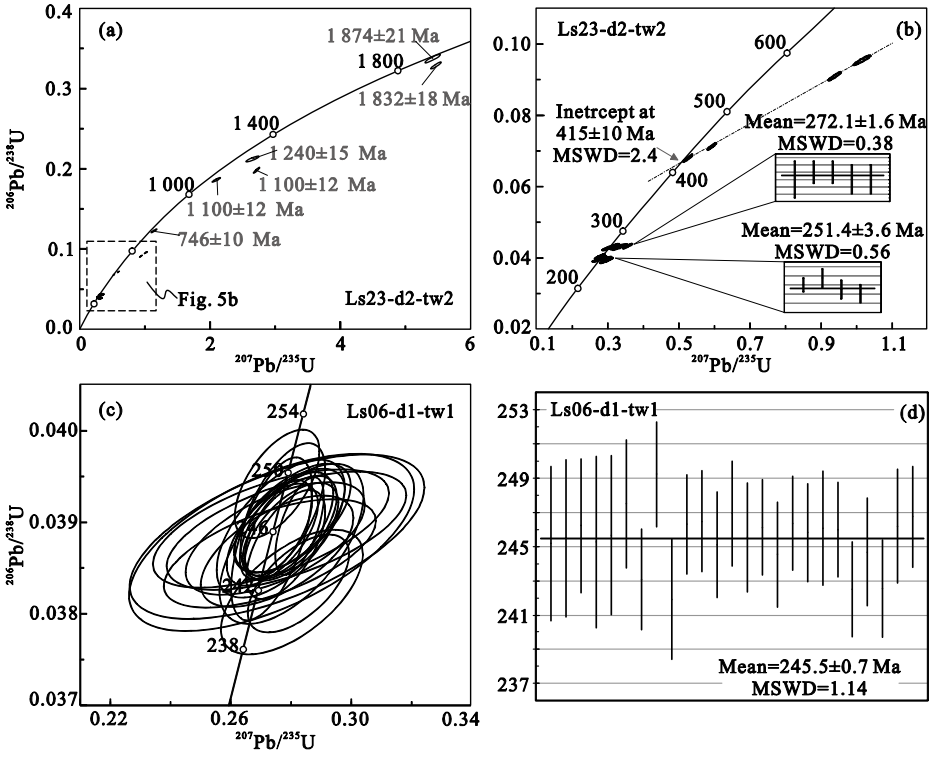

Figure 5. (a), (b) U-Pb concordia diagrams of zircon grains from the studied diabase sample Ls23-d2-tw2; (c) (d) monzogranite sample Ls06-d1-tw1. (b) shows the results of zircons with $^{206}Pb/^{238}U$ ages less than 600 Ma for Ls23-d2-tw2.

Table 2 Major oxide and trace elements composition of the studied diabases and monzogranites

Sample	Ls01-d1-q2	Ls01-d1-q10	Ls01-d1-q17	Ls01-d2-q7	Ls01-d2-q10	Ls01-d3-q5	Ls01-d1-q8	Ls01-d1-q14	Ls03-d6-q1	Ls06-d1-q1	Ls06-d3-q1	PM007D4-1GS	PM007D4-1W
Rock type	Diabase	Diabase	Diabase	Diabase	Diabase	Diabase	Diabase	Diabase	Diabase	Monzogranite	Monzogranite	Monzogranite	Monzogranite
Location	N41°25′29″ E106°54′15″	N41°25′32″ E106°54′10″	N41°25′39″ E106°54′14″	N41°25′41″ E106°53′52″	N41°25′41″ E106°53′50″	N41°26′01″ E106°53′42″	N41°25′31″ E106°54′11″	N41°25′35″ E106°54′07″	N41°26′18″ E106°54′36″	N41°26′16″ E106°44′30″	N41°25′56″ E106°44′01″	N41°25′32″ E106°44′25″	N41°25′32″ E106°44′25″
Major elements (wt.%)													
SiO_2	52.14	52.38	54.55	51.45	51.13	52.92	53.21	53.13	52.22	70.09	70.27	72.55	72.63
TiO_2	1.35	1.14	1.32	1.38	1.27	1.40	1.45	1.51	1.86	0.32	0.33	0.25	0.26
Al_2O_3	17.41	15.01	15.53	18.20	17.03	17.06	20.83	21.57	18.42	15.07	14.79	14.17	14.10
Fe_2O_3	7.90	2.61	2.53	2.89	2.39	2.51	2.06	2.40	8.18	1.30	1.39	0.99	1.00
FeO	1.00	5.68	5.15	5.42	5.79	5.57	4.60	3.15	1.06	1.08	1.02	0.65	0.70
MnO	0.12	0.12	0.11	0.12	0.12	0.13	0.09	0.07	0.12	0.05	0.05	0.02	0.03
MgO	5.75	9.66	7.53	5.58	6.66	5.26	3.01	2.27	3.78	0.86	0.87	0.40	0.42
CaO	8.00	7.81	6.63	8.88	8.72	7.62	7.91	7.65	7.02	2.26	2.28	1.37	1.40
Na_2O	3.82	2.56	3.34	3.36	3.55	4.09	4.11	4.07	4.23	4.08	3.98	4.07	4.06
K_2O	1.20	1.31	1.06	0.94	0.76	1.54	1.84	1.75	1.58	3.76	3.96	4.67	4.58
P_2O_5	0.18	0.17	0.18	0.18	0.16	0.20	0.24	0.24	0.31	0.10	0.11	0.07	0.08
LOI	1.82	1.77	2.27	1.83	2.55	1.91	0.84	2.34	2.01	1.38	1.22	0.81	0.77
Trace elements (ppm)													
Sc	22.1	22.0	20.7	25.9	25.7	27.0	15.1	15.2	19.8	4.1	4.6	2.7	2.8
V	128.0	145.0	132.0	121.0	149.0	161.0	102.0	100.0	128.0	23.0	31.5	36.3	37.7
Cr	59.2	494.0	268.0	82.4	158.0	139.0	62.4	53.6	66.3	4.7	8.3	5.7	5.8
Co	29.7	33.2	25.1	31.3	32.9	24.3	21.1	16.0	25.8	3.1	4.1	2.1	2.1
Ni	30.8	123.0	88.0	26.9	57.6	31.3	30.6	24.5	36.2	3.6	6.4	1.2	1.9
Cu	30.7	29.4	50.8	40.3	39.5	45.8	49.4	51.2	64.4	7.5	7.8	12.3	13.2
Zn	70.5	66.6	63.4	77.2	75.3	74.0	69.4	61.9	89.1	32.9	41.6	47.6	49.9
Ga	16.8	14.5	15.8	19.2	18.5	18.1	20.7	19.7	20.7	13.8	16.2	21.3	21.4
Cs	4.3	4.0	4.2	2.8	2.2	1.4	5.7	5.9	2.5	5.5	4.9	4.9	5.0
La	11.8	11.3	14.5	12.0	11.5	12.4	17.9	16.7	21.4	19.7	20.1	34.3	39.7
Ce	26.2	24.8	30.8	26.7	26.0	28.3	37.0	36.0	46.6	35.1	37.6	58.2	67.5
Pr	3.62	3.44	4.12	3.75	3.50	3.92	5.24	5.02	6.21	3.81	3.89	5.97	7.01
Nd	17.2	16.0	18.3	17.4	16.0	18.2	23.5	22.7	28.1	13.7	13.9	20.0	22.2
Sm	3.99	3.76	4.13	4.47	4.05	4.71	5.41	5.44	6.71	2.43	2.21	2.97	3.24
Eu	1.50	1.24	1.33	1.57	1.44	1.47	1.90	1.85	1.83	0.49	0.54	0.72	0.72

Table 2 Continued

Sample	Ls01-d1-q2	Ls01-d1-q10	Ls01-d1-q17	Ls01-d2-q7	Ls01-d2-q10	Ls01-d3-q5	Ls01-d1-q8	Ls01-d1-q14	Ls03-d6-q1	Ls06-d1-q1	Ls06-d3-q1	PM007D4-1GS	PM007D4-1W
Rock type	Diabase	Diabase	Diabase	Diabase	Diabase	Diabase	Diabase	Diabase	Diabase	Monzogranite	Monzogranite	Monzogranite	Monzogranite
Location	N41°25′29″ E106°54′15″	N41°25′32″ E106°54′10″	N41°25′39″ E106°54′14″	N41°25′41″ E106°53′52″	N41°25′41″ E106°53′50″	N41°26′01″ E106°53′42″	N41°25′31″ E106°54′11″	N41°25′35″ E106°54′07″	N41°26′18″ E106°54′36″	N41°26′16″ E106°44′30″	N41°25′56″ E106°44′01″	N41°25′32″ E106°44′25″	N41°25′32″ E106°44′25″
Trace elements (ppm)													
Gd	3.88	3.47	3.69	4.11	3.76	4.23	5.18	4.98	6.04	2.07	1.93	2.14	2.40
Tb	0.82	0.69	0.79	0.83	0.78	0.87	1.03	1.06	1.25	0.36	0.31	0.30	0.35
Dy	4.63	3.91	4.31	4.92	4.54	5.10	5.79	5.96	6.79	1.84	1.48	1.49	1.80
Ho	0.93	0.79	0.85	0.97	0.91	1.02	1.16	1.19	1.34	0.35	0.29	0.25	0.26
Er	2.60	2.26	2.49	2.77	2.55	2.86	3.27	3.37	3.78	1.07	0.85	0.68	0.76
Tm	0.44	0.37	0.40	0.45	0.44	0.46	0.52	0.55	0.60	0.16	0.15	0.10	0.10
Yb	2.72	2.31	2.51	2.81	2.72	2.97	3.22	3.34	3.87	1.15	1.01	0.60	0.70
Lu	0.39	0.33	0.35	0.38	0.36	0.40	0.45	0.46	0.50	0.17	0.16	0.09	0.10
Rb	35.5	48.1	44.1	40.4	29.9	73.2	83.2	71.7	72.2	109.0	128.0	169.0	173.0
Sr	339	287	343	413	352	405	438	391	398	310	383	320	324
Y	23.10	21.00	22.20	27.40	25.00	27.80	32.40	32.80	37.50	10.50	9.26	7.16	8.03
Zr	159	148	160	179	165	181	212	209	285	116	142	120	142
Nb	4.24	4.10	5.61	4.99	4.40	4.65	5.77	6.10	7.01	8.44	9.22	9.13	9.60
Ba	233	131	163	133	116	223	229	195	255	658	991	785	770
Hf	4.39	3.93	4.33	4.53	4.32	4.92	5.57	5.43	7.22	3.73	3.88	3.13	3.86
Ta	0.39	0.36	0.49	0.38	0.37	0.36	0.49	0.51	0.44	0.87	0.87	1.07	1.13
Pb	5.69	5.61	7.79	5.47	6.44	6.16	9.02	9.72	9.56	22.00	27.50	31.70	31.70
Th	2.77	2.41	3.48	2.62	2.74	2.98	4.27	4.28	5.60	8.69	8.87	22.20	25.60
U	0.74	0.62	0.92	1.24	0.78	0.83	1.90	1.27	1.75	1.92	1.50	1.45	1.76

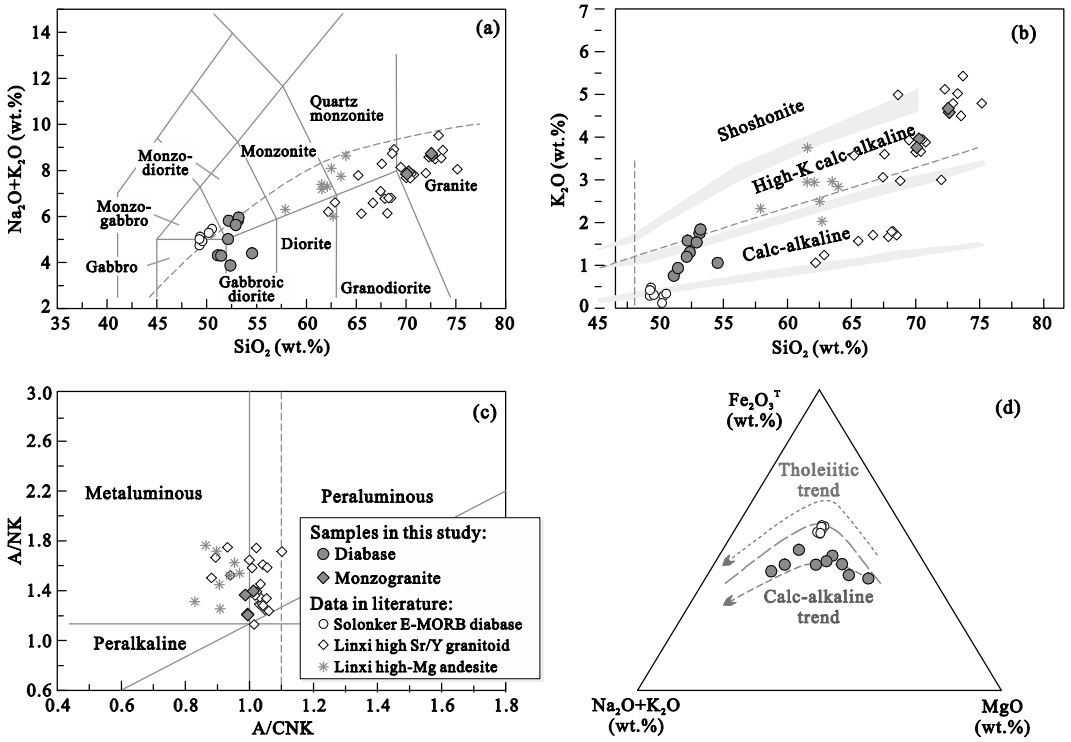

Figure 6. (a) TAS diagram (Middlemost, 1994; Irvine and Baragar, 1971); (b) K_2O vs. SiO_2 diagram (Rickwood, 1989); (c) A/NK vs. A/CNK diagram (Peccerillo and Taylor, 1976); (d) AFM diagram (Irvine and Baragar, 1971). The previously reported ~250 Ma Solonker E-MORB like diabases (Jian et al., 2010), the Linxi Triassic high-Mg adakitic andesites (Liu et al., 2012) and the Early–Middle Triassic High Sr/Y granitoids (Li et al., 2017) are plotted for comparison.

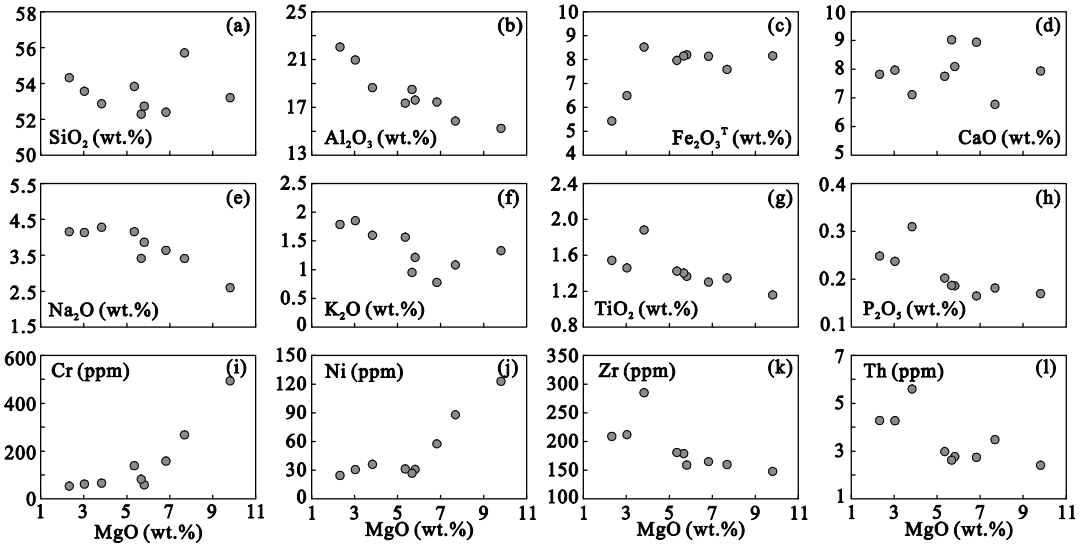

Figure 7. Harker diagrams of MgO vs. selected major and trace elements for the studied diabase samples.

contents, with high Sr/Y ratios (30–45) (Fig. 9). The monzogranites show notable enrichment in LREE ($(La/Yb)_N$=12.29–40.80) and slightly negative Eu anomalies (Eu/Eu*=0.66–0.88) in the chondrite-normalized diagram (Fig. 8a). Their primitive mantle-normalized trace element diagrams are generally characterized by enrichment in LILE, such as Rb, U and K, and depletion in Nb, Ta, Ti, and P (Fig. 8b). Overall, the monzogranites in this study display geochemical characteristics similar to those of the coeval adakitic rocks along the Solonker suture zone, such as the Early–Middle Triassic high Sr/Y granitoids in the Linxi area (Li et al., 2017) and the Early Triassic adakitic granitoids in the central Jilin area (Wang et al., 2015a).

3.3 Sr-Nd-Pb Isotopes

Detailed results of whole-rock Rb-Sr, Sm-Nd and Pb isotopes for the studied diabases are given in Table 3. Initial values of all the samples have been calculated based on their youngest concordant zircon U-Pb age of ~251 Ma. As shown in Fig. 10, the diabase samples have relatively variable initial $^{87}Sr/^{86}Sr$ values of 0.705 86 to 0.708 87 and $\varepsilon_{Nd}(t)$ values of -3.1 to +1.5, with Nd model ages ranging from 1 473 to 1 034 Ma, these characteristics are apparently different from the

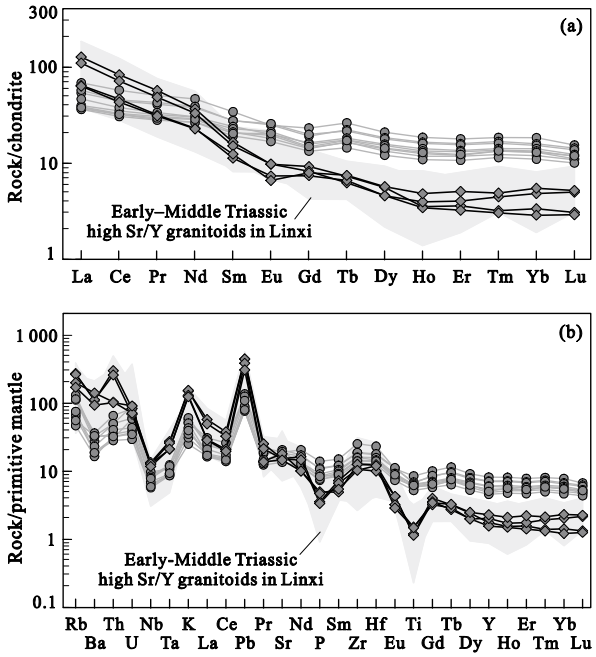

Figure 8. (a) Chondrite-normalized REE diagram and (b) primitive mantle-normalized trace element diagram for the studied diabase and monzogranite samples. The values of chondrite and primitive mantle are from Boynton (1984) and Sun and McDonough (1989), respectively. Data for the Early–Middle Triassic high Sr/Y granitoids in Linxi area are from Li et al. (2017).

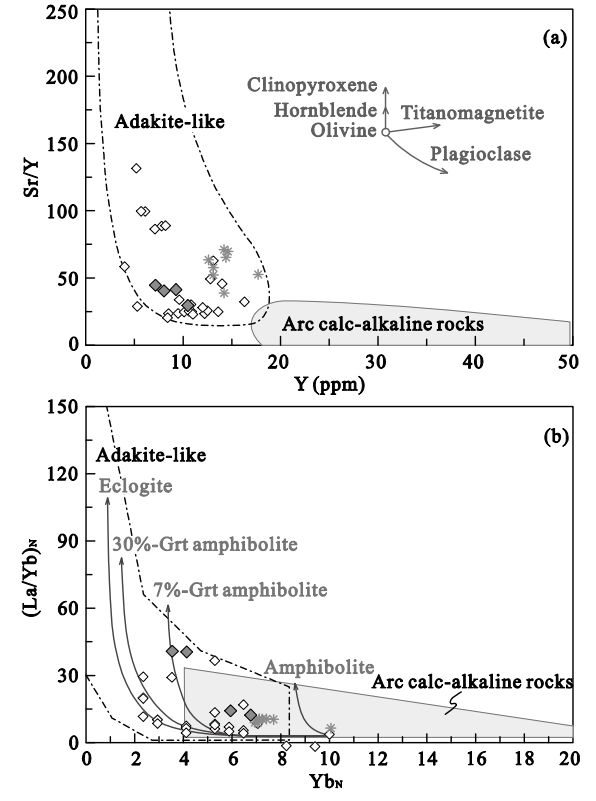

Figure 9. Adakite discrimination diagrams (a) Sr/Y vs. Y and (b) $(La/Yb)_N$ vs. Yb_N for the studied monzogranite samples. Fields for adakite and arc calc-alkaline rocks are based on Petford and Atherton (1996) and Defant and Drummond (1990). The crystal fractionation paths of the primary minerals in Fig. 9a are from Castillo et al. (1999). The batch partial melting trends in Fig. 9b are based on Petford and Atherton (1996).

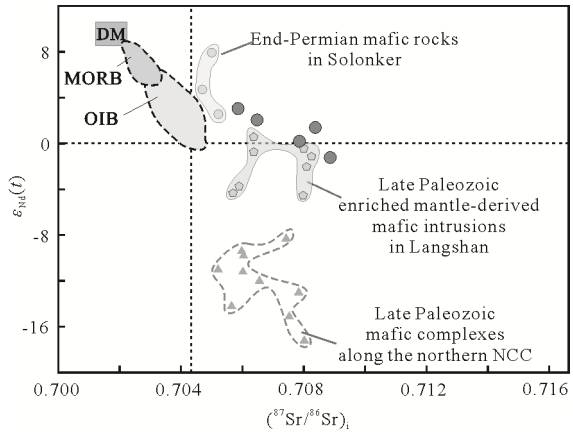

Figure 10. Plot of $\varepsilon_{Nd}(t)$ vs. $(^{87}Sr/^{86}Sr)_i$ for the studied diabase samples. The fields for DM (depleted mantle), MORB (middle ocean ridge basalt) and OIB (ocean island basalt) are from Zindler and Hart (1986). Data for the Late Paleozoic ultramafic-mafic complexes from the northern NCC are from Zhang et al. (2009b). Data for the Late Paleozoic enriched mantle-derived mafic intrusions in Langshan area and the end-Permian mafic rocks in the Solonker area are from Wang et al. (2015b) and Luo et al. (2016), respectively.

end-Permain mafic rocks in the Solonker area (Luo et al., 2016) and the Early Mesozoic ultramafic-mafic complexes along the northern NCC (Zhang et al., 2012), but similar to those of the Late Paleozoic enriched mantle-derived mafic intrusions in the region (Wang et al., 2015b). As for the Pb isotopic compositions, the initial ratios of $^{208}Pb/^{204}Pb$, $^{207}Pb/^{204}Pb$ and $^{206}Pb/^{204}Pb$ of the diabase samples vary from 35.968–37.346, 15.448–15.508 and 16.280–17.492, respectively, they plot above the North Hemisphere Reference Line (NHRL) and close to the compositional field of EM1 (Fig. 11).

3.4 Zircon Lu-Hf Isotopes

The zircon grains of monzogranite sample Ls06-d1-tw1 which were previously used for U-Pb age dating were also selected for Lu-Hf isotopes on the same spot. Individual Lu-Hf isotopic data, as well as the $^{206}Pb/^{238}U$ ages of the corresponding spots, are given in Table 4. Twenty analyses on zircons from sample Ls06-d1-tw1 yielded initial $^{176}Hf/^{177}Hf$ ratios of 0.281 896 to 0.282 373, their $\varepsilon_{Hf}(t)$ values and the corresponding T_{DM2} range from -25.8 to -8.8 (Fig. 12) and 2 900 to 1 833 Ma, respectively.

4 DISCUSSION

4.1 Petrogenesis of the Diabases

4.1.1 Formation age

Since the diabase dykes in this study are mostly hosted by the Late Paleozoic granitoids and unconformably covered by the Early Cretaceous Guyang Formation in the field, their formation ages can be roughly restricted to Late Paleozoic to Early Mesozoic. Besides, the pre-Mesozoic geological units in the Langshan area are pervasively deformed (Zhang et al., 2013; Darby and Ritts, 2007), whereas the studied diabases are undeformed and unmetamorphosed. Thus, the timing of the youngest deformation in the region can provide constraint on the upper age limit of the studied diabase. As reported by Lin et al. (2014), the Early Permian (~290 Ma) granitic porphyries in

Urad Houqi are generally characterized by NE-striking and N-vergent orientations and structures, and they are the youngest deformed intrusions in the Langshan area, which implies that the diabase dykes in this study must have been formed after Early Permian.

Although zircons are volumetrically minor in mafic-ultramafic magma and zircon grains obtained from the mafic-ultramafic rocks are mostly captured, previous studies have shown that high-precision zircon U-Pb dating remains useful in placing constraints on the formation ages of mafic-ultramafic rocks (e.g., Yu et al., 2017; Zhang et al., 2009b). Our U-Pb dating results indicate that the zircon $^{206}Pb/^{238}U$ ages acquired from diabase sample Ls23-d2-tw2 are varying from 248 to 1 874 Ma. The older ages may be xenocrysts that potentially captured during the magma ascent, but nine relatively younger zircons yielded two weighted mean $^{206}Pb/^{238}U$ ages of ~272 and ~251 Ma (Fig. 5b). Considering that the Early Permian igneous rocks are widely distributed in the southwestern XMOB (e.g., Wang et al., 2015b; Lin et al., 2014; Peng et al., 2013; Zhang et al., 2009a), we propose that the weighted mean age of ~272 Ma was more likely to be in relation to the Early Permian magmatism in the region. The four zircons with ages of ~251 Ma are relatively larger in size and exhibit developed oscillatory zoning in the CL images (Fig. 4), these features are more akin to those of zircons from the intermediate-felsic magmatic rocks instead of the mafic magma, suggesting that the studied diabase probably formed after ~251 Ma. Moreover, previous studies show that extensive Middle–Late Triassic magmatism (including the Middle Triassic high Sr/Y monzogranite in this study) was developed in southwestern XMOB (e.g., Zhang et al., 2014a and references therein). However, no Middle–Late Triassic zircon is observed in sample Ls23-d2-tw2, which means that the studied diabase is unlikely to be formed after Middle–Late Triassic. Consequently, we assume that Early Triassic, which is slightly older than the studied monzogranite (245.5±0.7 Ma), might be the best estimate of the formation age of the diabases.

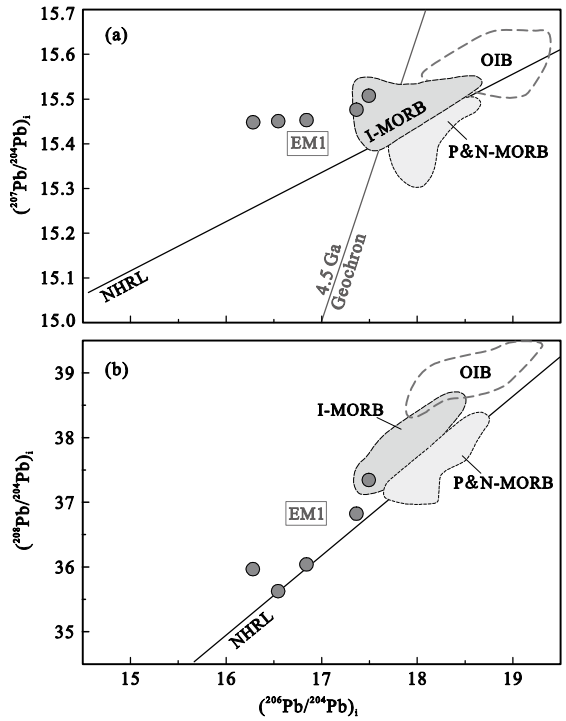

Figure 11. (a) $(^{206}Pb/^{204}Pb)_i$ vs. $(^{207}Pb/^{204}Pb)_i$ and (b) $(^{206}Pb/^{204}Pb)_i$ vs. $(^{208}Pb/^{204}Pb)_i$ diagrams for the studied diabase samples. The fields for I-MORB (Indian MORB), P & N-MORB (Pacific and North Atlantic MORB), OIB, EM1, NHLR and the 4.5 Ga geochron are from Zou et al. (2000), Zindler and Hart (1986) and Hart (1984).

Table 3 Whole rocks Sr-Nd-Pb isotopic data for the studied diabase samples

Sample	Ls01-d1-2	Ls01-d1-8	Ls01-d1-17	Ls01-d2-7	Ls03-d6-1
Rb (μg/g)	39.46	86.87	48.36	39.51	75.61
Sr (μg/g)	376.9	452.3	385	412.1	414.1
$^{87}Rb/^{86}Sr$	0.301 8	0.553 9	0.362 2	0.276 3	0.526 5
$^{87}Sr/^{86}Sr$	0.707 56	0.709 84	0.710 16	0.706 85	0.710 26
1δ	0.000	0.000	0.000	0.000	0.000
$(^{87}Sr/^{86}Sr)_i$	0.706	0.707	0.708	0.705	0.708
Sm (μg/g)	5.13	5.474	4.319	4.163	6.707
Nd (μg/g)	20.3	23.24	18.58	16.6	28.42
$^{147}Sm/^{144}Nd$	0.152 9	0.142 5	0.140 6	0.151 7	0.142 8
$^{143}Nd/^{144}Nd$	0.512	0.512	0.512 48	0.512	0.512
1δ	0.000	0.000	0.000	0.000	0.000
$(^{143}Nd/^{144}Nd$	0.512	0.512	0.512	0.512	0.512
$\varepsilon_{Nd}(t)$	2.06	0.19	-1.23	3.05	1.4
T_{DM} (Ma)	1 076	1 158	1 283	1 473	1 034
Pb (μg/g)	5.47	1.54	3	1.38	3.12
U (μg/g)	0.97	0.58	0.8	0.55	1.55
Th (μg/g)	2.89	2.17	2.79	2.21	5.09
$^{206}Pb/^{204}Pb$	18.508	18.524	18.48	18.591	18.587
$^{207}Pb/^{204}Pb$	15.55	15.533	15.52	15.523	15.545
$^{208}Pb/^{204}Pb$	38.523	38.549	38.438	38.429	38.603
$(^{206}Pb/^{204}Pb)_i$	17.492	16.841	17.363	16.544	16.28
$(^{207}Pb/^{204}Pb)_i$	15.508	15.453	15.476	15.451	15.448
$(^{208}Pb/^{204}Pb)_i$	37.346	36.042	36.825	35.628	35.968

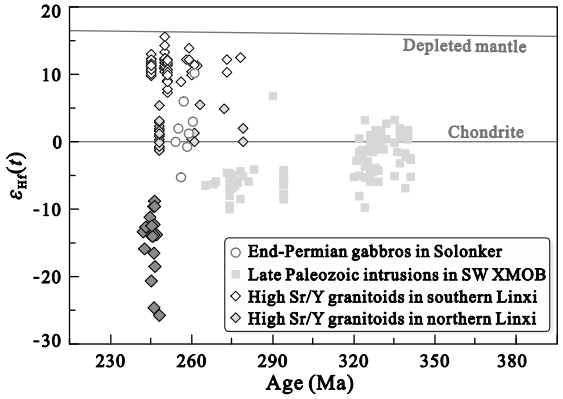

Figure 12. Zircon $\varepsilon_{Hf}(t)$ vs. U-Pb age diagram for the studied monzogranite sample Ls06-d1-tw1. Data source for the Triassic high Sr/Y granitoids in northern and southern Linxi area are from Li et al. (2017). The end-Permian gabbros in Solonker (Luo et al., 2016) and the Late Paleozoic intrusions in SW XMOB (Liu et al., 2016; Peng et al., 2013; Pi et al., 2010) are also shown for comparison.

Table 4 Zircon Lu-Hf isotopic compositions of the studied monzogranite sample Ls06-d1-tw1

Sample spot	Age (Ma)	$^{176}Hf/^{177}Hf$	2σ	$^{176}Lu/^{177}Hf$	2σ	$^{176}Yb/^{177}Hf$	2σ	$\varepsilon_{Hf}(t)$	T_{DM1} (Ma)	T_{DM2} (Ma)	$f_{Lu/Hf}$
Ls06-d1-tw1.01	245	0.282 271	0.000 024	0.020 840	0.000 081	0.000 859	0.000 003	-12.5	1 379	2 064	-0.97
Ls06-d1-tw1.02	246	0.282 227	0.000 019	0.024 826	0.000 150	0.000 958	0.000 006	-14.0	1 444	2 163	-0.97
Ls06-d1-tw1.03	246	0.282 351	0.000 019	0.015 781	0.000 135	0.000 623	0.000 005	-9.6	1 260	1 883	-0.98
Ls06-d1-tw1.04	246	0.282 373	0.000 017	0.013 352	0.000 114	0.000 550	0.000 005	-8.8	1 227	1 833	-0.98
Ls06-d1-tw1.05	248	0.281 896	0.000 020	0.034 959	0.000 328	0.001 350	0.000 012	-25.8	1 923	2 900	-0.96
Ls06-d1-tw1.06	243	0.282 267	0.000 018	0.015 929	0.000 048	0.000 665	0.000 002	-12.6	1 378	2 073	-0.98
Ls06-d1-tw1.07	242	0.282 247	0.000 020	0.017 003	0.000 428	0.000 685	0.000 016	-13.4	1 406	2 118	-0.98
Ls06-d1-tw1.08	246	0.281 930	0.000 020	0.036 772	0.000 395	0.001 405	0.000 014	-24.6	1 879	2 827	-0.96
Ls06-d1-tw1.09	246	0.282 232	0.000 016	0.018 090	0.000 126	0.000 729	0.000 005	-13.8	1 428	2 148	-0.98
Ls06-d1-tw1.10	245	0.282 229	0.000 017	0.017 079	0.000 140	0.000 683	0.000 005	-13.9	1 431	2 156	-0.98
Ls06-d1-tw1.11	247	0.282 232	0.000 020	0.016 948	0.000 131	0.000 691	0.000 005	-13.8	1 427	2 148	-0.98
Ls06-d1-tw1.12	246	0.282 228	0.000 020	0.015 719	0.000 280	0.000 638	0.000 011	-13.9	1 430	2 157	-0.98
Ls06-d1-tw1.13	245	0.282 306	0.000 020	0.013 909	0.000 099	0.000 565	0.000 004	-11.2	1 320	1 983	-0.98
Ls06-d1-tw1.14	246	0.282 100	0.000 019	0.021 041	0.000 066	0.000 838	0.000 003	-18.5	1 616	2 445	-0.97
Ls06-d1-tw1.15	246	0.282 351	0.000 018	0.013 326	0.000 214	0.000 527	0.000 008	-9.6	1 257	1 883	-0.98
Ls06-d1-tw1.16	246	0.282 275	0.000 022	0.014 781	0.000 150	0.000 585	0.000 005	-12.3	1 364	2 053	-0.98
Ls06-d1-tw1.17	246	0.282 155	0.000 021	0.018 748	0.000 121	0.000 748	0.000 004	-16.5	1 535	2 320	-0.98
Ls06-d1-tw1.18	243	0.282 175	0.000 019	0.016 144	0.000 044	0.000 668	0.000 002	-15.9	1 504	2 277	-0.98
Ls06-d1-tw1.19	245	0.282 040	0.000 019	0.024 647	0.000 176	0.000 986	0.000 007	-20.7	1 704	2 578	-0.97
Ls06-d1-tw1.20	246	0.282 239	0.000 019	0.016 306	0.000 111	0.000 650	0.000 004	-13.6	1 416	2 134	-0.98

The Langshan Early Triassic diabase, together with the recently identified coeval mafic rocks in Wengunshan (Lin et al., 2014), Mandula area (Jian et al., 2010) and Solonker area (Luo et al., 2016; Jian et al., 2010), indicate the presence of the end-Permian to Early Triassic magmatic flare-up in southwestern XMOB.

4.1.2 Crustal contamination and fractional crystallization

Presence of the Archean and Proterozoic zircon grains (Fig. 5a), together with the positive Zr-Hf-Pb and negative Nb-Ta anomalies in the primitive mantle-normalized diagram of the diabase samples (Fig. 8b), indicate that the parental magma may have undergone crustal contamination during magma ascent. However, all the diabases are mafic with low concentrations of SiO_2 (51.13 wt.%–54.55 wt.%) and relatively high $Mg^{\#}$ values (43.2–68.2), suggesting that bulk crustal contamination is unlikely. Their low Lu/Yb ratios (0.13–0.14), narrow range of $(Th/Yb)_N$ values (5.41–8.39), consistent LREE and LILE distribution patterns (Fig. 8), as well as relatively high $\varepsilon_{Nd}(t)$ values (-3.1 to +1.5), are also inconsistent with significant crustal contamination. Besides, significant crustal contamination would result in linear correlations between $Mg^{\#}$ values and $\varepsilon_{Nd}(t)$ values, $(Th/Nb)_N$ and Nb/La ratios, but such characteristics are not observed the diabase samples. Thus, crustal contamination, although it cannot be ruled out, does not appear to play a significant role in the petrogenesis of the studied diabases.

The diabase samples have variable MgO (2.27 wt.%–9.66 wt.%), Ni (24.5 ppm–123 ppm) and Cr (53.6 ppm–494 ppm) contents, indicating that fractional crystallization might have occurred prior to their emplacement. In the Harker diagram (Fig. 7), the positive correlations between MgO and $Fe_2O_3^T$, Cr and Ni and the negative correlations between MgO and SiO_2 indicate considerable degree of fractionation of olivine and/or clinopyroxene. The increasing TiO_2 with decreasing MgO, together with the relatively consistent CaO contents imply that the parental magmas only underwent a minor degree of clinopyroxene fractionation (Figs. 7d and 7g). Although Al_2O_3 is negatively correlated with MgO (Fig. 7b), the negligible Sr and Eu anomalies (Fig. 8) suggest that plagioclase fractionation was insignificant. Moreover, the roughly negative correlations between MgO and TiO_2, P_2O_5 (Fig. 7), along with the negligible Ti anomalies (Fig. 8b), argue against significant fractionation of the Fe-Ti oxides and apatite. Therefore, olivine with a minor amount of clinopyroxene are the major fractionated minerals of the studied diabases.

4.1.3 Nature of mantle sources

Overall, all the diabase samples have similar trace element and Sr-Nd-Pb isotopic characteristics, so their derivation can be ascribed to a common magma source. The low SiO_2 contents (51.13 wt.%–54.55 wt.%) and relatively high MgO, Cr, Ni contents suggest that they were likely originated from mantle-derived components rather than a crustal source (e.g., Rapp et al., 2003). Isotopically, these rocks display relatively high initial ratios of $^{87}Sr/^{86}Sr$ (0.705 9–0.708 9), with $\varepsilon_{Nd}(t)$ values and Nd model ages respectively ranging from -3.1 to +1.5 (Fig. 10) and 1 473 to 1 034 Ma, implying an enriched lithospheric mantle source. This is also consistent with their relatively high initial ratios of $^{208}Pb/^{204}Pb$ (35.968–37.346), $^{207}Pb/^{204}Pb$ (15.448–15.508) and $^{206}Pb/^{204}Pb$ (16.280–17.492).

Arc-like geochemical signatures, such as enrichment in LREE and LILE relative to heavy REE (HREE) and HFSE, are

generally related to either extensively crustal contamination or partial melting of an enriched mantle source (e.g., Zhang et al., 2011). As significant crustal contamination can be excluded, the "arc-like" trace element patterns (Fig. 8) and the enriched isotopic signatures (Fig. 10) of the studied diabase were therefore mainly inherited from an enriched lithospheric mantle source. Depletion of HFSE in the primitive mantle normalized diagrams is generally caused by fluid-related and/or melt-related metasomatism in subduction process (e.g., Ma et al., 2014; Duggen et al., 2005; Thirlwall et al., 1994). Thus, we propose that the mantle source of the studied diabase may have been modified by subduction-related fluids and/or melt. Furthermore, the LILE enriched geochemical features are calling for a LILE-enriched mantle source, which means that volatile-bearing minerals (such as phlogopite and amphibole) might be the major host phases in the mantle source origin (e.g., Ionov et al., 1997; Foley et al., 1996). Since melts in equilibrium with amphibole generally have significantly lower Rb/Sr (<0.1) and higher Ba/Rb (>20) ratios, whereas melts of phlogopite-bearing source are expected to show significantly lower Ba/Rb ratios (Ma et al., 2014; Furman and Graham, 1999). The relatively low Ba/Rb ratios (2.72–6.56) and variable Rb/Sr ratios (0.08–0.19) of the diabases in this study indicate predominance of phlogopite in their mantle source (Fig. 13a), implying that metasomatism by volatile-rich melts must have occurred prior to the partial melting. Moreover, partial melting in the spinel-stability field generally has low Dy/Yb ratios (<1.5), while melting in the garnet-stability field shows much higher Dy/Yb ratios (>2.5) (e.g., Ma et al., 2014). The diabase samples in this study have Dy/Yb ratios ranging from 1.67 to 1.80, indicating that the partial melting was probably operated within the spinel-garnet transition zone lherzolite (Ma et al., 2014; Jiang et al., 2010; Duggen et al., 2005). However, the relatively low Ce/Y (0.97–1.39) and $(Tb/Yb)_N$ ratios (1.31–1.45) of the diabase samples indicate that the melts were more likely to be derived from a spinel-stability mantle source (McKenzie and Bickle, 1988). In the Sm/Yb vs. La/Sm and Lu/Hf vs. Sm/Nd diagrams, all the diabase samples plot closed to the 1%–5% partial melting curve of spinel facies (Figs. 13b–13c), indicating that parental magma of the diabases were likely derived from the low degree partial melting of the phlogopite- bearing lherzolite in the spinel-stability field. Compared with the coeval enriched lithospheric mantle derived mafic rocks in the Solonker area (Jian et al., 2010), the diabases in this study have relatively lower $\varepsilon_{Nd}(t)$ values (-3.1–+1.5), older Nd model ages (1 473–1 034 Ma) and variable initial $^{87}Sr/^{86}Sr$ ratios (0.705 9–0.708 9) (Fig. 10). Such isotopic characteristics might point to a relatively heterogeneous SCLM (subcontinental lithospheric mantle) source beneath the southwestern XMOB.

4.2 Petrogenesis of the Monzogranites

The monzogranite samples in this study are characterized by high Sr/Y (30–45) and La/Yb ratios (Fig. 9), with relatively high Al_2O_3 (14.15 wt.%–15.98 wt.%) and Sr (310 ppm–380 ppm) contents and low Y (7.16 ppm–10.50 ppm) and Yb (0.60 ppm–1.15 ppm) contents, indicating geochemical characteristics of adakite-like rocks (Martin et al., 2005; Defant and Drummond, 1990). Generally, adakite or adakite-like rocks can

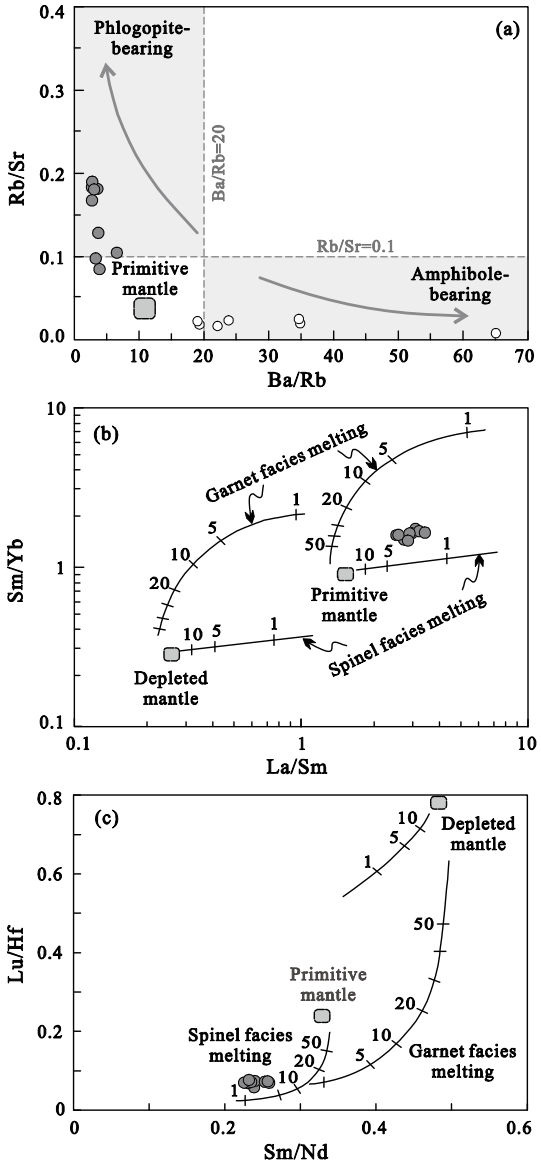

Figure 13. (a) Ba/Rb vs. Rb/Sr (Furman and Graham, 1999), (b) Sm/Yb vs. La/Sm, and (c) Lu/Hf vs. Sm/Nd diagrams for the studied diabase samples. The melting curves in Figs. 13b and 13c are from Zhao and Asimow (2014).

be generated by the partial melting of subducted oceanic slab (e.g., Defant and Drummond, 1990), the partial melting of delaminated lower crust (Wang et al., 2006; Kay and Kay, 1993), the partial melting of thickened lower crust (Chung et al., 2003; Atherton and Petford, 1993) and the differentiation of parental basaltic magmas (Castillo, 2012; Prouteau and Scaillet, 2003).

The studied monzogranites possess high SiO_2 (70.09 wt.%–72.63 wt.%), low MgO (0.40 wt.%–0.87 wt.%), Cr (4.74 ppm–8.31 ppm) and Ni (1.15 ppm–6.35 ppm) contents, these features are more akin to the thickened lower crust-derived adakites and metabasaltic and eclogite experimental melts (Fig. 14) (Wang et al., 2006), rather than the subducted oceanic slab-derived or delaminated lower crust-derived adakites (Martin et al., 2005). Their uniform geochemistry, together with the absence of mafic minerals (e.g., amphibole and clinopyroxene), do not support an origin from primary basaltic magma by crustal

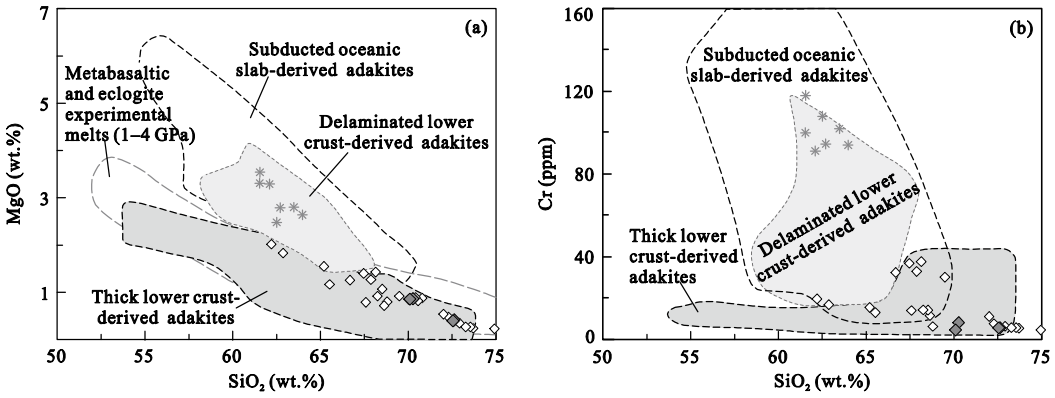

Figure 14. (a) MgO vs. SiO_2 and (b) Cr vs. SiO_2 diagrams for the studied monzogranites. Fields for the subducted oceanic slab-derived adakites, delaminated lower crust-derived adakites, thick lower crust-derived adakites and metabasaltic and eclogite experimental melts (1–4 GPa) are after Wang et al. (2006). The Triassic high-Mg adakitic andesites (Liu et al., 2012) and Early–Middle Triassic high Sr/Y granitoids (Li et al., 2017) in the Linxi area are also plotted for comparison.

assimilation and fractional crystallization processes (Castillo et al., 1999). However, the relatively flat HREE patterns (Fig. 8a), as well as the high Zr/Sm ratios (40–64) of these monzogranite samples suggest amphibole-dominated residual phases in the source region, which is consistent with the coeval high Sr/Y granitoids in the Linxi area (Li et al., 2017). Thus, these rocks are unlikely to be originated from a significantly thickened lower crust. Recent partial melting experiments show that adakite-like magmas can also be produced by the low degree partial melting (10%–40%) of a slightly thickened mafic lower crust with *P-T* condition of 1–1.25 Gpa and 800–950 ºC (corresponding to a depth of 30–40 km) (Qian and Hermann, 2013). Considering that only moderate thickening of the crust (40–45 km) occurred during the final orogenic evolution in the southern CAOB (Li et al., 2017, 2016a; Zhang et al., 2014b), we propose that the low degree partial melting of the moderately thickened lower crust is likely to be a plausible explanation for the genesis of the studied high Sr/Y monzogranites.

As shown in the $\varepsilon_{Hf}(t)$ vs. U-Pb age diagram (Fig. 12), the Early–Middle high Sr/Y granitoids in northern Linxi have positive zircon $\varepsilon_{Hf}(t)$ values of +7.3 to +15.6, while those in southern Linxi have weak negative to positive zircon $\varepsilon_{Hf}(t)$ values of -1.3 to +5.4 (Li et al., 2017). These characteristics are apparently different from the Middle Triassic high Sr/Y monzogranites in this study, which are characterized by negative zircon $\varepsilon_{Hf}(t)$ values (-25.8 to -8.8) and old T_{DM2} model ages (2 900–1 833 Ma). This kind of spatial distribution may indicate that the lower crust source region of the Early–Middle Triassic high Sr/Y rocks in the southwestern XMOB was dominated by ancient crustal materials, the source region south of the Solonker suture zone got a greater contribution from juvenile crustal materials, whereas the area north of the Solonker suture zone was dominated by juvenile components.

4.3 Tectonic Implications

The final closure of the Paleo-Asian Ocean and the final continental amalgamation/collision were suggested to begin with the initial collision between the SMT and the NCC during the Middle Permian (e.g., Li et al., 2017, 2016a, 2014; Xiao et al., 2015; Jian et al., 2010), leading to the cessation of the arc magmatism and marine sedimentation, accompanied by a short magmatic hiatus and a regional angular unconformity in the XMOB (Li et al., 2016b, 2014; Eizenhöfer et al., 2014). Afterwards, the terminal collision triggered a regional greenschist-blueschist facies metamorphism along the Solonker suture zone in the Late Permian (Li et al., 2017, 2016a; Jian et al., 2010), which marks the onset of the final episode of orogenic evolution in the XMOB.

As stated above, the Early Triassic diabases in this study were derived from the enriched lithospheric mantle source beneath the southwestern XMOB. Considering that subduction of the Paleo-Asian Ocean had ceased since the Middle–Late Permian, we assume that the slab break-off following the terminal collision was a plausible mechanism for the generation of the studied diabases. Slab break-off can significantly increase the temperature of the overlying lithosphere due to the upwelling of the hot asthenosphere through the slab window, leading to partial melting of the overlying lithospheric mantle, as well as crustal anatexis (e.g., van de Zedde and Wortel, 2001). Likewise, Jian et al. (2010) suggested that the end-Permian to Early Triassic igneous rocks (255–250 Ma) in the Mandula forearc mélange were derived from the decompression melting of mantle peridotite by heat from the upwelling asthenosphere during the slab break-off. Li et al. (2016a) also proposed that the end-Permian to Early Triassic magmatic flare-up in the southeastern Xilinhot area was in response to the final slab break-off in the XMOB.

The Middle Triassic high Sr/Y monzogranites in this study, combined with the Early–Middle Triassic high Sr/Y granitoids in Linxi area (Li et al., 2017) and central Jilin (Wang et al., 2015a), indicate moderate thickening and shortening of the crust. Thus, considerable contraction must have occurred after the slab break-off, which might be in relation to the ongoing convergence between the NCC and the SMT. The heat from the underplated basaltic magma may lead to: (1) partial melting of the moderately thickened ancient lower crust beneath the southwestern XMOB to generate high Sr/Y magma with negative $\varepsilon_{Hf}(t)$ values, and (2) partial melting of the moderately thickened juvenile lower crust beneath the Solonker suture zone to produce high Sr/Y magma with positive $\varepsilon_{Hf}(t)$ values. In

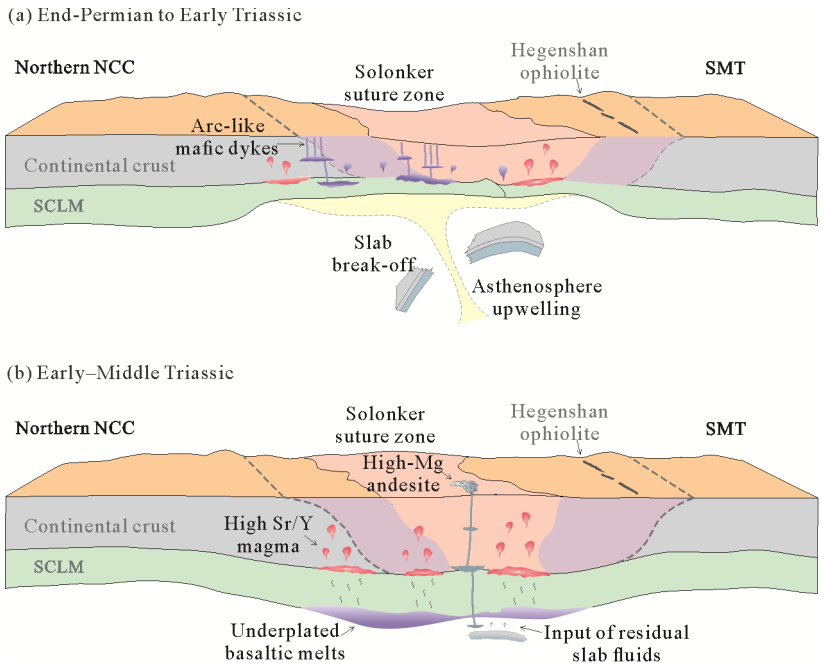

Figure 15. Schematic illustrations showing the genesis model and geodynamic environment of end-Permian to Early–Middle Triassic magmatism during the final orogenic evolution of the XMOB. SCLM. Sub-continental lithospheric mantle.

addition, recent studies revealed that the aqueous fluids released from an residual oceanic slab in the upper mantle also had participated in the generation of the Early–Middle Triassic high Sr/Y magmatism along the Solonker suture zone (Li et al., 2017; Song et al., 2015; Zhang et al., 2014b; Liu et al., 2012; Jian et al., 2010).

The Paleozoic tectonic development of the XMOB was overall dominated by the evolution of the Paleo-Asian Ocean between the NCC and the SMT (e.g., Eizenhöfer et al., 2015, 2014; Xiao et al., 2015, 2003; Windley et al., 2007). During Carboniferous to Early Permian, the progressively double-sided subduction of the Paleo-Asian Ocean enabled an Andean-style continental margins to develop on the northern NCC and the SMT (Liu et al., 2013; Chen et al., 2009; Zhang et al., 2009a; Xiao et al., 2003), accompanied by extensive arc magmatism (e.g., Li et al., 2016b; Chen et al., 2009; Zhang et al., 2009a). The initial collision between the NCC and SMT in Middle Permian prevented further oceanic subduction and terminated the arc-related magmatism. The Paleo-Asian Ocean in the XMOB ultimately closed during the Late Permian, leading to the formation of the Solonker suture zone (Li et al., 2017; Xiao et al., 2015; Jian et al., 2010; Zhang et al., 2009a). The slab break-off of the Paleo-Asian oceanic lithosphere switched the regionally tectonic regime from the prolonged compression to a temporary extension, and then resulted in the magmatic flare-up during end-Permian to Early Triassic (Fig. 15a), such as the Langshan diabase dykes in this study, the E-MORB diabase, sanukitoid, high-Mg diorite and anorthosite in the Solonker ophiolitic mélanges (Jian et al., 2010), as well as those collision-related calc-alkaline granitoids in the southeastern Xilinhot area (Li et al., 2016a). Subsequently, the ongoing weak convergence between the NCC and the SMT initiated moderately crustal thickening and uplift, generating the Early–Middle Triassic high Sr/Y magmas and the high-Mg adakitic andesites (Fig. 15b) (Li et al., 2017; Liu et al., 2012). The post-orogenic extension in the XMOB might be started in the Late Triassic, as evidenced by the 224–208 Ma metamorphic core complex in the Sonid Zuoqi area (Davis et al., 2004), as well as the widespread A-type granitic rocks and alkaline complexes along the northern NCC (Zhang et al., 2014a, 2012). By the end of Early Mesozoic, tectonic evolution of the XMOB was overall controlled by the Mongol-Okhotsk tectonic regime to the northwest and the Paleo-Pacific tectonic regime to the east (e.g., Zhou and Wilde, 2013).

5 CONCLUSIONS

(1) The studied diabases and monzogranites were respectively formed during Early Triassic and Middle Triassic, corresponding to the end-Permian to Early–Middle Triassic magmatic events identified in the southwestern XMOB.

(2) The Early Triassic diabases were derived from the low degree partial melting of a subduction-metasomatized lithospheric mantle followed by fractionation of olivine and minor clinopyroxene, the Middle Triassic monzogranites were generated by the low degree partial melting of a moderately thickened ancient lower crust.

(3) The diabases were resulted from the slab break-off of the Paleo-Asian oceanic lithosphere following the terminal collision between the NCC and the SMT in the southwestern XMOB, while the monzogranites were resulted from the subsequently crustal thickening and uplift.

ACKNOWLEDGMENTS

This study was jointly supported by the Geological Survey of China (No. 1212011085490) and the National Natural Science Foundation of China (No. 41421002). We sincerely thank the editors and the anonymous reviewers for their critical and constructive comments. We are grateful to Guangqiang Xiong,

Hongtao Zhao, Quanliu Chen, and Zhong Wang for their help with the field work. We thank Yu Zhu, Fangyi Zhang and Zezhong Zhang for their laboratory assistance. We also appreciate Yuan Yuan and Yaoyao Zhang for their insightful suggestions. The final publication is available at Springer via https://doi.org/10.1007/s12583-019-1015-5.

REFERENCES CITED

Andersen, T., 2002. Correction of Common Lead in U-Pb Analyses that do not Report ^{204}Pb. *Chemical Geology*, 192(1/2): 59–79. https://doi.org/10.1016/s0009-2541(02)00195-x

Atherton, M. P., Petford, N., 1993. Generation of Sodium-Rich Magmas from Newly Underplated Basaltic Crust. *Nature*, 362(6416): 144–146. https://doi.org/10.1038/362144a0

Bao, Z. A., Chen, L., Zong, C. L., et al., 2017. Development of Pressed Sulfide Powder Tablets for *in situ* Sulfur and Lead Isotope Measurement Using LA-MC-ICP-MS. *International Journal of Mass Spectrometry*, 421: 255–262. https://doi.org/10.1016/j.ijms.2017.07.015

Boynton, W. V., 1984. Cosmochemistry of the Rare Earth Elements: Meteorite Studies. In: Henderson, P. E., ed., Rare Earth Element Geochemistry. Elsevier, Amsterdam. 63–114

Castillo, P. R., 2012. Adakite Petrogenesis. *Lithos*, 134/135(3): 304–316. https://doi.org/10.1016/j.lithos.2011.09.013

Castillo, P. R., Janney, P. E., Solidum, R. U., 1999. Petrology and Geochemistry of Camiguin Island, Southern Philippines: Insights to the Source of Adakites and Other Lavas in a Complex Arc Setting. *Contributions to Mineralogy and Petrology*, 134(1): 33–51. https://doi.org/10.1007/s004100050467

Cawood, P. A., Kröner, A., Collins, W. J., et al., 2009. Accretionary Orogens through Earth History. *Geological Society*, *London*, *Special Publications*, 318(1): 1–36. https://doi.org/10.1144/sp318.1

Chen, B., Ma, X. H., Liu, A. K., et al., 2009. Zircon U-Pb Ages of the Xilinhot Metamorphic Complex and Blueschist and Implications for Tectonic Evolution of the Solonker Suture. *Acta Petrologica Sinica*, 25(12): 3123–3129 (in Chinese with English Abstract)

Chung, S. L., Liu, D. Y., Ji, J. Q., et al., 2003. Adakites from Continental Collision Zones: Melting of Thickened Lower Crust beneath Southern Tibet. *Geology*, 31(11): 1021–1024. https://doi.org/10.1130/g19796.1

Condie, K. C., Belousova, E., Griffin, W. L., et al., 2009. Granitoid Events in Space and Time: Constraints from Igneous and Detrital Zircon Age Spectra. *Gondwana Research*, 15(3/4): 228–242. https://doi.org/10.1016/j.gr.2008.06.001

Darby, B. J., Ritts, B. D., 2007. Mesozoic Structural Architecture of the Lang Shan, North-Central China: Intraplate Contraction, Extension, and Synorogenic Sedimentation. *Journal of Structural Geology*, 29(12): 2006–2016. https://doi.org/10.1016/j.jsg.2007.06.011

Davis, G. A., Xu, B., Zheng, Y. D., et al., 2004. Indosinian Extension in the Solonker Suture Zone: The Sonid Zuoqi Metamorphic Core Complex, Inner Mongolia, China. *Earth Science Frontiers*, 11(3): 135–143. https://doi.org/10.1007/bf02873097

de Jong, K., Xiao, W., Windley, B. F., et al., 2006. Ordovician ^{40}Ar/^{39}Ar Phengite Ages from the Blueschist-Facies Ondor Sum Subduction-Accretion Complex (Inner Mongolia) and Implications for the Early Paleozoic History of Continental Blocks in China and Adjacent Areas. *American Journal of Science*, 306(10): 799–845. https://doi.org/10.2475/10.2006.02

Defant, M. J., Drummond, M. S., 1990. Derivation of some Modern Arc Magmas by Melting of Young Subducted Lithosphere. *Nature*, 347(6294): 662–665. https://doi.org/10.1038/347662a0

Duggen, S., Hoernle, K., van den Bogaard, P., et al., 2005. Post-Collisional Transition from Subduction- to Intraplate-Type Magmatism in the Westernmost Mediterranean: Evidence for Continental-Edge Delamination of Subcontinental Lithosphere. *Journal of Petrology*, 46(6): 1155–1201. https://doi.org/10.1093/petrology/egi013

Eizenhöfer, P. R., Zhao, G. C., Zhang, J., et al., 2014. Final Closure of the Paleo-Asian Ocean along the Solonker Suture Zone: Constraints from Geochronological and Geochemical Data of Permian Volcanic and Sedimentary Rocks. *Tectonics*, 33(4): 441–463. https://doi.org/10.1002/2013tc003357

Eizenhöfer, P. R., Zhao, G. C., Zhang, J., et al., 2015. Geochemical Characteristics of the Permian Basins and Their Provenances Across the Solonker Suture Zone: Assessment of Net Crustal Growth during the Closure of the Palaeo-Asian Ocean. *Lithos*, 224/225: 240–255. https://doi.org/10.1016/j.lithos.2015.03.012

Ferrari, L., 2004. Slab Detachment Control on Mafic Volcanic Pulse and Mantle Heterogeneity in Central Mexico. *Geology*, 32(1): 77. https://doi.org/10.1130/g19887.1

Foley, S. F., Jackson, S. E., Fryer, B. J., et al., 1996. Trace Element Partition Coefficients for Clinopyroxene and Phlogopite in an Alkaline Lamprophyre from Newfoundland by LAM-ICP-MS. *Geochimica et Cosmochimica Acta*, 60(4): 629–638. https://doi.org/10.1016/0016-7037(95)00422-x

Furman, T., Graham, D., 1999. Erosion of Lithospheric Mantle beneath the East African Rift System: Geochemical Evidence from the Kivu Volcanic Province. *Lithos*, 48(1/2/3/4): 237–262. https://doi.org/10.1016/s0024-4937(99)00031-6

Gao, S., Liu, X. M., Yuan, H. L., et al., 2002. Determination of Forty Two Major and Trace Elements in USGS and NIST SRM Glasses by Laser Ablation-Inductively Coupled Plasma-Mass Spectrometry. *Geostandards and Geoanalytical Research*, 26(2): 181–196. https://doi.org/10.1111/j.1751-908x.2002.tb00886.x

Hart, S. R., 1984. A Large-Scale Isotope Anomaly in the Southern Hemisphere Mantle. *Nature*, 309(5971): 753–757. https://doi.org/10.1038/309753a0

Hoskin, P. W. O., Schaltegger, U., 2003. The Composition of Zircon and Igneous and Metamorphic Petrogenesis. *Reviews in Mineralogy and Geochemistry*, 53(1): 27–62. https://doi.org/10.2113/0530027

Hu, J. M., Gong, W. B., Wu, S. J., et al., 2014. LA-ICP-MS Zircon U-Pb Dating of the Langshan Group in the Northeast Margin of the Alxa Block, with Tectonic Implications. *Precambrian Research*, 255: 756–770. https://doi.org/10.1016/j.precamres.2014.08.013

Ionov, D. A., Griffin, W. L., O'Reilly, S. Y., 1997. Volatile-Bearing Minerals and Lithophile Trace Elements in the Upper Mantle. *Chemical Geology*, 141(3/4): 153–184. https://doi.org/10.1016/s0009-2541(97)00061-2

Irvine, T. N., Baragar, W. R. A., 1971. A Guide to the Chemical Classification of the Common Volcanic Rocks. *Canadian Journal of Earth Sciences*, 8(5): 523–548. https://doi.org/10.1139/e71-055

Jahn, B. M., Wu, F. Y., Chen, B., 2000. Granitoids of the Central Asian Orogenic Belt and Continental Growth in the Phanerozoic. *Transactions of the Royal Society of Edinburgh*: *Earth Sciences*, 91(1/2): 181–193. https://doi.org/10.1017/s0263593300007367

Jian, P., Liu, D. Y., Kröner, A., et al., 2008. Time Scale of an Early to Mid-Paleozoic Orogenic Cycle of the Long-Lived Central Asian Orogenic Belt, Inner Mongolia of China: Implications for Continental Growth. *Lithos*, 101(3/4): 233–259. https://doi.org/10.1016/j.lithos.2007.07.005

Jian, P., Liu, D. Y., Kröner, A., et al., 2010. Evolution of a Permian Intrao-

ceanic Arc-Trench System in the Solonker Suture Zone, Central Asian Orogenic Belt, China and Mongolia. *Lithos*, 118(1/2): 169–190. https://doi.org/10.1016/j.lithos.2010.04.014

Jiang, Y. H., Jiang, S. Y., Ling, H. F., et al., 2010. Petrogenesis and Tectonic Implications of Late Jurassic Shoshonitic Lamprophyre Dikes from the Liaodong Peninsula, NE China. *Mineralogy and Petrology*, 100(3/4): 127–151. https://doi.org/10.1007/s00710-010-0124-8

Kay, R. W., Kay, S. M., 1993. Delamination and Delamination Magmatism. *Tectonophysics*, 219(1/2/3): 177–189. https://doi.org/10.1016/0040-1951(93)90295-u

Li, H. K., Geng, J. Z., Hao, S., et al., 2009. The Study of Zircon U-Pb Dating by Means LA-MC-ICPMS. *Bulletin of Mineralogy*, *Petrology and Geochemistry*, 28(Suppl.): 77 (in Chinese)

Li, S., Chung, S. L., Wilde, S. A., et al., 2016a. Linking Magmatism with Collision in an Accretionary Orogen. *Scientific Reports*, 6(1): 25751. https://doi.org/10.1038/srep25751

Li, S., Wilde, S. A., Wang, T., et al., 2016b. Latest Early Permian Granitic Magmatism in Southern Inner Mongolia, China: Implications for the Tectonic Evolution of the Southeastern Central Asian Orogenic Belt. *Gondwana Research*, 29(1): 168–180. https://doi.org/10.1016/j.gr.2014.11.006

Li, S., Chung, S. L., Wilde, S. A., et al., 2017. Early–Middle Triassic High Sr/Y Granitoids in the Southern Central Asian Orogenic Belt: Implications for Ocean Closure in Accretionary Orogens. *Journal of Geophysical Research*: *Solid Earth*, 163(6): 2291–2309. https://doi.org/10.1002/2017jb014006

Li, S., Wilde, S. A., He, Z. H., et al., 2014. Triassic Sedimentation and Postaccretionary Crustal Evolution along the Solonker Suture Zone in Inner Mongolia, China. *Tectonics*, 33(6): 960–981. https://doi.org/10.1002/2013tc003444

Lin, L. N., Xiao, W. J., Wan, B., et al., 2014. Geochronologic and Geochemical Evidence for Persistence of South-Dipping Subduction to Late Permian Time, Langshan Area, Inner Mongolia (China): Significance for Termination of Accretionary Orogenesis in the Southern Altaids. *American Journal of Science*, 314(2): 679–703. https://doi.org/10.2475/02.2014.08

Liu, J. F., Li, J. Y., Chi, X. G., et al., 2013. A Late-Carboniferous to Early Early-Permian Subduction-Accretion Complex in Daqing Pasture, Southeastern Inner Mongolia: Evidence of Northward Subduction beneath the Siberian Paleoplate Southern Margin. *Lithos*, 177: 285–296. https://doi.org/10.1016/j.lithos.2013.07.008

Liu, M., Zhang, D., Xiong, G. Q., et al., 2016. Zircon U-Pb Age, Hf Isotope and Geochemistry of Carboniferous Intrusions from the Langshan Area, Inner Mongolia: Petrogenesis and Tectonic Implications. *Journal of Asian Earth Sciences*, 120: 139–158. https://doi.org/10.1016/j.jseaes.2016.01.005

Liu, Y. S., Wang, X. H., Wang, D. B., et al., 2012. Triassic High-Mg Adakitic Andesites from Linxi, Inner Mongolia: Insights into the Fate of the Paleo-Asian Ocean Crust and Fossil Slab-Derived Melt-Peridotite Interaction. *Chemical Geology*, 328: 89–108. https://doi.org/10.1016/j.chemgeo.2012.03.019

Liu, Y., 2012. Geochemical and Chronological Characteristics of the Granitic Gneisses and Intrusive Rocks from Dongshengmiao Region, Inner Mongolia and Their Tectonic Implications: [Dissertation]. Lanzhou University, Lanzhou. 21–46 (in Chinese)

Ludwig, K. R., 2003. ISOPLOT 3.0: A Geochronological Toolkit for Microsoft Excel. Geochronology Center: Special Publication, Berkeley. 4

Luo, Z. W., Xu, B., Shi, G. Z., et al., 2016. Solonker Ophiolite in Inner Mongolia, China: A Late Permian Continental Margin-Type Ophiolite. *Lithos*, 261: 72–91. https://doi.org/10.1016/j.lithos.2016.03.001

Ma, L., Jiang, S. Y., Hofmann, A. W., et al., 2014. Lithospheric and Asthenospheric Sources of Lamprophyres in the Jiaodong Peninsula: A Consequence of Rapid Lithospheric Thinning beneath the North China Craton?. *Geochimica et Cosmochimica Acta*, 124: 250–271. https://doi.org/10.1016/j.gca.2013.09.035

Ma, S. W., Liu, C. F., Xu, Z. Q., et al., 2017. Geochronology, Geochemistry and Tectonic Significance of the Early Carboniferous Gabbro and Diorite Plutons in West Ujimqin, Inner Mongolia. *Journal of Earth Science*, 28(2): 249–264. https://doi.org/10.1007/s12583-016-0912-2

Martin, H., Smithies, R. H., Rapp, R., et al., 2005. An Overview of Adakite, Tonalite-Trondhjemite-Granodiorite (TTG), and Sanukitoid: Relationships and some Implications for Crustal Evolution. *Lithos*, 79(1/2): 1–24. https://doi.org/10.1016/j.lithos.2004.04.048

McKenzie, D., Bickle, M. J., 1988. The Volume and Composition of Melt Generated by Extension of the Lithosphere. *Journal of Petrology*, 29(3): 625–679. https://doi.org/10.1093/petrology/29.3.625

Miao, L. C., Fan, W. M., Liu, D. Y., et al., 2008. Geochronology and Geochemistry of the Hegenshan Ophiolitic Complex: Implications for Late-Stage Tectonic Evolution of the Inner Mongolia-Daxinganling Orogenic Belt, China. *Journal of Asian Earth Sciences*, 32(5/6): 348–370. https://doi.org/10.1016/j.jseaes.2007.11.005

Middlemost, E. A. K., 1994. Naming Materials in the Magma/Igneous Rock System. *Earth-Science Reviews*, 37(3/4): 215–224. https://doi.org/10.1016/0012-8252(94)90029-9

Peccerillo, A., Taylor, S. R., 1976. Geochemistry of Eocene Calc-Alkaline Volcanic Rocks from the Kastamonu Area, Northern Turkey. *Contributions to Mineralogy and Petrology*, 58(1): 63–81. https://doi.org/10.1007/bf00384745

Peng, R. M., Zhai, Y. S., Li, C. S., et al., 2013. The Erbutu Ni-Cu Deposit in the Central Asian Orogenic Belt: A Permian Magmatic Sulfide Deposit Related to Boninitic Magmatism in an Arc Setting. *Economic Geology*, 108(8): 1879–1888. https://doi.org/10.2113/econgeo.108.8.1879

Peng, R. M., Zhai, Y. S., Wang, J. P., et al., 2010. Discovery of Neoproterozoic Acid Volcanic Rock in the South-Western Section of Langshan, Inner Mongolia. *Chinese Science Bulletin*, 55(26): 2611–2620 (in Chinese with English Abstract)

Petford, N., Atherton, M., 1996. Na-Rich Partial Melts from Newly Underplated Basaltic Crust: The Cordillera Blanca Batholith, Peru. *Journal of Petrology*, 37(6): 1491–1521. https://doi.org/10.1093/petrology/37.6.1491

Pi, Q. H., Liu, C. Z., Chen, Y. L., et al., 2010. Formation Epoch and Genesis of Intrusive Rocks in Huogeqi Ore Field of Inner Mongolia and Their Relationship with Copper Mineralization. *Mineral Deposits*, 29(3): 437–451 (in Chinese with English Abstract)

Prouteau, G., Scaillet, B., 2003. Experimental Constraints on the Origin of the 1991 Pinatubo Dacite. *Journal of Petrology*, 44(12): 2203–2241. https://doi.org/10.1093/petrology/egg075

Qian, Q., Hermann, J., 2013. Partial Melting of Lower Crust at 10–15 kbar: Constraints on Adakite and TTG Formation. *Contributions to Mineralogy and Petrology*, 165(6): 1195–1224. https://doi.org/10.1007/s00410-013-0854-9

Rapp, R. P., Shimizu, N., Norman, M. D., 2003. Growth of Early Continental Crust by Partial Melting of Eclogite. *Nature*, 425(6958): 605–609. https://doi.org/10.1038/nature02031

Rickwood, P. C., 1989. Boundary Lines within Petrologic Diagrams Which Use Oxides of Major and Minor Elements. *Lithos*, 22(4): 247–263. https://doi.org/10.1016/0024-4937(89)90028-5

Robinson, P. T., Zhou, M. F., Hu, X. F., et al., 1999. Geochemical Con-

straints on the Origin of the Hegenshan Ophiolite, Inner Mongolia, China. *Journal of Asian Earth Sciences*, 17(4): 423–442. https://doi.org/10.1016/s1367-9120(99)00016-4

Schulmann, K., Paterson, S., 2011. Asian Continental Growth. *Nature Geoscience*, 4(12): 827–829. https://doi.org/10.1038/ngeo1339

Song, S. G., Wang, M. M., Xu, X., et al., 2015. Ophiolites in the Xing'an-Inner Mongolia Accretionary Belt of the CAOB: Implications for Two Cycles of Seafloor Spreading and Accretionary Orogenic Events. *Tectonics*, 34(10): 2221–2248. https://doi.org/10.1002/2015tc003948

Sun, S. S., McDonough, W. F., 1989. Chemical and Isotopic Systematics of Oceanic Basalts: Implications for Mantle Composition and Processes. *Geological Society*, *London*, *Special Publications*, 42(1): 313–345. https://doi.org/10.1144/gsl.sp.1989.042.01.19

Thirlwall, M. F., Smith, T. E., Graham, A. M., et al., 1994. High Field Strength Element Anomalies in Arc Lavas: Source or Process?. *Journal of Petrology*, 35(3): 819–838. https://doi.org/10.1093/petrology/35.3.819

van de Zedde, D. M. A., Wortel, M. J. R., 2001. Shallow Slab Detachment as a Transient Source of Heat at Midlithospheric Depths. *Tectonics*, 20(6): 868–882. https://doi.org/10.1029/2001tc900018

Wang, Q., Xu, J. F., Jian, P., et al., 2006. Petrogenesis of Adakitic Porphyries in an Extensional Tectonic Setting, Dexing, South China: Implications for the Genesis of Porphyry Copper Mineralization. *Journal of Petrology*, 47(1): 119–144. https://doi.org/10.1093/petrology/egi070

Wang, Z. J., Xu, W. L., Pei, F. P., et al., 2015a. Geochronology and Geochemistry of Middle Permian–Middle Triassic Intrusive Rocks from Central-Eastern Jilin Province, NE China: Constraints on the Tectonic Evolution of the Eastern Segment of the Paleo-Asian Ocean. *Lithos*, 238: 13–25. https://doi.org/10.1016/j.lithos.2015.09.019

Wang, Z. Z., Han, B. F., Feng, L. X., et al., 2015b. Geochronology, Geochemistry and Origins of the Paleozoic–Triassic Plutons in the Langshan Area, Western Inner Mongolia, China. *Journal of Asian Earth Sciences*, 97: 337–351. https://doi.org/10.1016/j.jseaes.2014.08.005

Wang, Z. Z., Han, B. F., Feng, L. X., et al., 2016. Tectonic Attribution of the Langshan Area in Western Inner Mongolia and Implications for the Neoarchean–Paleoproterozoic Evolution of the Western North China Craton: Evidence from LA-ICP-MS Zircon U-Pb Dating of the Langshan Basement. *Lithos*, 261: 278–295. https://doi.org/10.1016/j.lithos.2016.03.005

Wilde, S. A., 2015. Final Amalgamation of the Central Asian Orogenic Belt in NE China: Paleo-Asian Ocean Closure versus Paleo-Pacific Plate Subduction—A Review of the Evidence. *Tectonophysics*, 662: 345–362. https://doi.org/10.1016/j.tecto.2015.05.006

Windley, B. F., Alexeiev, D., Xiao, W. J., et al., 2007. Tectonic Models for Accretion of the Central Asian Orogenic Belt. *Journal of the Geological Society*, 164(1): 31–47. https://doi.org/10.1144/0016-76492006-022

Xiao, W. J., Windley, B. F., Hao, J., et al., 2003. Accretion Leading to Collision and the Permian Solonker Suture, Inner Mongolia, China: Termination of the Central Asian Orogenic Belt. *Tectonics*, 22(6): 1–8. https://doi.org/10.1029/2002tc001484

Xiao, W. J., Windley, B. F., Sun, S., et al., 2015. A Tale of Amalgamation of Three Permo-Triassic Collage Systems in Central Asia: Oroclines, Sutures, and Terminal Accretion. *Annual Review of Earth and Planetary Sciences*, 43(1): 477–507. https://doi.org/10.1146/annurev-earth-060614-105254

Xu, B., Charvet, J., Chen, Y., et al., 2013. Middle Paleozoic Convergent Orogenic Belts in Western Inner Mongolia (China): Framework, Kinematics, Geochronology and Implications for Tectonic Evolution of the Central Asian Orogenic Belt. *Gondwana Research*, 23(4): 1342–1364. https://doi.org/10.1016/j.gr.2012.05.015

Yu, Y., Sun, M., Huang, X. L., et al., 2017. Sr-Nd-Hf-Pb Isotopic Evidence for Modification of the Devonian Lithospheric Mantle beneath the Chinese Altai. *Lithos*, 284/285: 207–221. https://doi.org/10.1016/j.lithos.2017.04.004

Yuan, H. L., Gao, S., Dai, M. N., et al., 2008. Simultaneous Determinations of U-Pb Age, Hf Isotopes and Trace Element Compositions of Zircon by Excimer Laser-Ablation Quadrupole and Multiple-Collector ICP-MS. *Chemical Geology*, 247(1/2): 100–118. https://doi.org/10.1016/j.chemgeo.2007.10.003

Yuan, H. L., Gao, S., Liu, X. M., et al., 2004. Accurate U-Pb Age and Trace Element Determinations of Zircon by Laser Ablation-Inductively Coupled Plasma-Mass Spectrometry. *Geostandards and Geoanalytical Research*, 28(3): 353–370. https://doi.org/10.1111/j.1751-908x.2004.tb00755.x

Yuan, W., Yang, Z. Y., 2015. The Alashan Terrane was not Part of North China by the Late Devonian: Evidence from Detrital Zircon U-Pb Geochronology and Hf Isotopes. *Gondwana Research*, 27(3): 1270–1282. https://doi.org/10.1016/j.gr.2013.12.009

Zeng, Q. D., Yang, J. H., Zhang, Z. L., et al., 2013. Petrogenesis of the Yangchang Mo-Bearing Granite in the Xilamulun Metallogenic Belt, NE China: Geochemistry, Zircon U-Pb Ages and Sr-Nd-Pb Isotopes. *Geological Journal*, 49(1): 1–14. https://doi.org/10.1002/gj.2481

Zhang, J. R., Wei, C. J., Chu, H., et al., 2016a. Mesozoic Metamorphism and Its Tectonic Implication along the Solonker Suture Zone in Central Inner Mongolia, China. *Lithos*, 261: 262–277. https://doi.org/10.1016/j.lithos.2016.03.014

Zhang, J., Zhang, B. H., Zhao, H., 2016b. Timing of Amalgamation of the Alxa Block and the North China Block: Constraints Based on Detrital Zircon U-Pb Ages and Sedimentologic and Structural Evidence. *Tectonophysics*, 668/669: 65–81. https://doi.org/10.1016/j.tecto.2015.12.006

Zhang, J., Li, J. Y., Xiao, W. J., et al., 2013. Kinematics and Geochronology of Multistage Ductile Deformation along the Eastern Alxa Block, NW China: New Constraints on the Relationship between the North China Plate and the Alxa Block. *Journal of Structural Geology*, 57: 38–57. https://doi.org/10.1016/j.jsg.2013.10.002

Zhang, S. H., Zhao, Y., Davis, G. A., et al., 2014a. Temporal and Spatial Variations of Mesozoic Magmatism and Deformation in the North China Craton: Implications for Lithospheric Thinning and Decratonization. *Earth-Science Reviews*, 131: 49–87. https://doi.org/10.1016/j.earscirev.2013.12.004

Zhang, S. H., Gao, R., Li, H. Y., et al., 2014b. Crustal Structures Revealed from a Deep Seismic Reflection Profile Across the Solonker Suture Zone of the Central Asian Orogenic Belt, Northern China: An Integrated Interpretation. *Tectonophysics*, 612/613: 26–39. https://doi.org/10.1016/j.tecto.2013.11.035

Zhang, S. H., Zhao, Y., Ye, H., et al., 2014c. Origin and Evolution of the Bainaimiao Arc Belt: Implications for Crustal Growth in the Southern Central Asian Orogenic Belt. *Geological Society of America Bulletin*, 126(9/10): 1275–1300. https://doi.org/10.1130/b31042.1

Zhang, S. H., Zhao, Y., Song, B., et al., 2009a. Contrasting Late Carboniferous and Late Permian–Middle Triassic Intrusive Suites from the Northern Margin of the North China Craton: Geochronology, Petrogenesis, and Tectonic Implications. *Geological Society of America Bulletin*, 121: 181–200. https://doi.org/10.1130/b26157.1

Zhang, S. H., Zhao, Y., Liu, X. C., et al., 2009b. Late Paleozoic to Early Mesozoic Mafic-Ultramafic Complexes from the Northern North China Block: Constraints on the Composition and Evolution of the Lithospheric Mantle. *Lithos*, 110(1/2/3/4): 229–246.

https://doi.org/10.1016/j.lithos.2009.01.008

Zhang, S. H., Zhao, Y., Ye, H., et al., 2012. Early Mesozoic Alkaline Complexes in the Northern North China Craton: Implications for Cratonic Lithospheric Destruction. *Lithos*, 155: 1–18. https://doi.org/10.1016/j.lithos.2012.08.009

Zhang, X. B., Wang, K. Y., Wang, C. Y., et al., 2017. Age, Genesis, and Tectonic Setting of the Mo-W Mineralized Dongshanwan Granite Porphyry from the Xilamulun Metallogenic Belt, NE China. *Journal of Earth Science*, 28(3): 433–446. https://doi.org/10.1007/s12583-016-0934-1

Zhang, X. H., Mao, Q., Zhang, H. F., et al., 2011. Mafic and Felsic Magma Interaction during the Construction of High-K Calc-Alkaline Plutons within a Metacratonic Passive Margin: The Early Permian Guyang Batholith from the Northern North China Craton. *Lithos*, 125(1/2): 569–591. https://doi.org/10.1016/j.lithos.2011.03.008

Zhao, J. H., Asimow, P. D., 2014. Neoproterozoic Boninite-Series Rocks in South China: A Depleted Mantle Source Modified by Sediment-Derived Melt. *Chemical Geology*, 388: 98–111. https://doi.org/10.1016/j.chemgeo.2014.09.004

Zhao, X. C., Zhou, W. X., Fu, D., et al., 2018. Isotope Chronology and Geochemistry of the Lower Carboniferous Granite in Xilinhot, Inner Mongolia, China. *Journal of Earth Science*, 29(2): 280–294. https://doi.org/10.1007/s12583-017-0942-2

Zhou, J. B., Wilde, S. A., 2013. The Crustal Accretion History and Tectonic Evolution of the NE China Segment of the Central Asian Orogenic Belt. *Gondwana Research*, 23(4): 1365–1377. https://doi.org/10.1016/j.gr.2012.05.012

Zindler, A., Hart, S. R., 1986. Chemical Geodynamics. *Annual Review of Earth and Planetary Sciences*, 14(1): 493–571. https://doi.org/10.1146/annurev.ea.14.050186.002425

Zou, H. B., Zindler, A., Xu, X. S., et al., 2000. Major, Trace Element, and Nd, Sr and Pb Isotope Studies of Cenozoic Basalts in SE China: Mantle Sources, Regional Variations, and Tectonic Significance. *Chemical Geology*, 171(1/2): 33–47. https://doi.org/10.1016/s0009-2541(00)00243-6